

Spin-Density-Wave Gap with Dirac Nodes and Two-Magnon Raman Scattering in BaFe_2As_2

Shunji Sugai^{*1,2,3}, Yuki Mizuno^{1,3}, Ryoutarou Watanabe^{3,4}, Takahiko Kawaguchi^{3,4}, Koshi Takenaka^{3,4}, Hiroshi Ikuta^{3,4}, Yasumasa Takayanagi¹, Naoki Hayamizu¹, and Yasuhiro Sone¹

¹*Department of Physics, Faculty of Science, Nagoya University, Furo-cho, Chikusa-ku, Nagoya 464-8602, Japan*

²*Department of Physics, Arts and Science, Petroleum Institute, P.O.Box 2533, Abu Dhabi, UAE*

³*TRIP, Japan Science and Technology Agency (JST), Chiyoda, Tokyo 102-0075, Japan*

⁴*Department of Crystalline Materials Science, Nagoya University, Furo-cho, Chikusa-ku, Nagoya 464-8603, Japan*

Raman selection rules for electronic and magnetic excitations in BaFe_2As_2 were theoretically investigated and applied them to the separate detection of the nodal and anti-nodal gap excitations at the spin density wave (SDW) transition and the separate detection of the nearest and the next nearest neighbor exchange interaction energies. Raman spectra are composed of magnetic excitations with gradually decreasing intensity toward far above the SDW transition temperature (T_{SDW}) and electronic excitations induced by the Brillouin zone folding below T_{SDW} . The SDW gap has Dirac nodes, because many orbitals participate in the electronic states near the Fermi energy. Using a two-orbital band model the electronic excitations near the Dirac node and the anti-node are found to have different symmetries. Applying the symmetry difference to Raman scattering the nodal and anti-nodal electronic excitations are separately obtained. The low-energy spectra from the anti-nodal region have critical fluctuation just above T_{SDW} and change into the gap structure by the first order transition at T_{SDW} , while those from the nodal region gradually change into the SDW state. Magnetic excitations are observed as a very broad peak in all polarization configurations. The selection rule for two-magnon scattering from the stripe spin structure was obtained. Applying it to the two-magnon Raman spectra it is found that the magnetic exchange interaction energies are not presented by the short-range superexchange model, but the second derivative of the total energy of the stripe spin structure with respect to the moment directions. The selection rule and the peak energy are expressed by the two-magnon scattering process in an insulator, but the large spectral weight above twice the maximum spin wave energy is difficult to explain by the decayed spin wave. It may be explained by the electronic scattering of itinerant carriers with the magnetic self-energy in the localized spin picture or the particle-hole excitation model in the itinerant spin picture. The magnetic scattering spectra are compared to the insulating and metallic cuprate superconductors whose spins are believed to be localized.

KEYWORDS: BaFe_2As_2 , SDW gap, Dirac node, Two-magnon Raman scattering

1. Introduction

Two-dimensional iron pnictides form a new family of superconductors with the transition temperature up to $T_c = 55 \text{ K}$.^{1,2} The BaFe_2As_2 family undergoes superconducting state when the spin density wave (SDW) is suppressed by substituting the element³⁻⁵

*E-mail address: sugai.shunji@h.mbox.nagoya-u.ac.jp, ssugai@pi.ac.ae

or pressurizing.⁶ Quasi-static magnetic measurement shows the disappearance of the spin order and magnetic excitations above the spin density wave transition temperature T_{SDW} or in the metallic phase. However, the lost spin order is only perpendicular to the two-dimensional layer⁷ and the high-energy magnetic excitations in the layer clearly remains above T_{SDW} or in the metallic phase as observed in magnetic Raman scattering and neutron scattering.⁸⁻¹² It strongly suggests that the superconductivity is induced by the same magnetic correlation as in the SDW state.

The magnetism of iron pnictide cannot be simply understood by the localized or itinerant spin model, because the magnetic moment $M = 0.8 \sim 0.9\mu_B/\text{Fe}$ is intermediate.^{10,13-18} The SDW phase is usually stabilized by the decrease of the electronic energy by opening of the gap at the Fermi energy in the folded bands. In the iron pnictide the SDW is not simply explained by the energy gain due to the gap formation induced by the Fermi surface nesting between the hole pocket at the Γ point and the electron pocket at the M point in k space. The spin structure is consistent with the Fermi surface nesting in BaFe_2As_2 ,¹⁹⁻²³ but not in FeTe , because the spin stripe direction is different by 45° .^{24,25} Johannes and Mazin¹⁶ pointed out that the energy gain is mainly one-electron energy balance for the antiferromagnetic (AF) spin patterns. The energy gain by the nesting is only a part of it. In fact a full SDW gap does not open in BaFe_2As_2 as known from the fact that the electric conductivity in the SDW state is even better than in the normal state. It is caused by the remaining Dirac nodes.²⁶⁻²⁹ Furthermore the magnetic exchange interaction energies are not simply obtained from the conventional short-range superexchange mechanism.³⁰⁻³⁴ The exchange interactions are very different, if they are obtained from the total energy of the long-range stripe spin structure. The exchange interaction in the y direction is antiferromagnetic in the former case, but ferromagnetic in the latter case.

BaFe_2As_2 undergoes the SDW state by the first order transition^{9,17,35-39} accompanied by the tetragonal ($I4/mmm$)-orthorhombic ($Fmmm$) structural transition at $T_{\text{SDW}} = 137$ K.^{4,17,40} The magnetic order in the SDW state is a stripe type in which nearest-neighbor spins are antiparallel in the x direction and parallel in the y direction.^{10,13,14,30,40,41} In this article we use the a and b axes as the tetragonal crystallographic axes and the x and y axes as the orthorhombic axes which are rotated by 45° from the a and b axes.

The electronic states in the SDW state is different from the conventional one. Usually the SDW state is insulating, because a full SDW gap opens at the Fermi energy. Despite

the SDW state, BaFe_2As_2 is metallic because electronic states remain at the Fermi energy (E_F). It is expressed by the selective inter-orbital coupling in the multi-orbital bands of BaFe_2As_2 .^{20,42–44} Wang *et al.*²⁶ and Ran *et al.*²⁷ predicted the nodal gaps composed of point-contact Dirac cones. The theoretical works of the Dirac nodes were reported^{26–29,45,46} and some of them showed that the Dirac nodes are protected.^{26–29} Angle-resolved photoemission spectroscopy (ARPES) observed the Dirac nodes near E_F .⁴⁷ The k -linear dispersion of the Dirac cone is expressed by the massless relativistic Weyl equation²⁹ which expresses the motion of a neutrino. It is known that the two-dimensional massless Dirac Fermion exhibits a variety of unusual phenomena.⁴⁸ For example, the interaction to the acoustic phonon is very weak, causing a very large mobility.

In order to find out whether the gap excitations near the Dirac node and the anti-node were separately detected, the orbital components in the electron and the hole bands were calculated in the two-dimensional two-orbital tight band model. The most area of the band in the k_x - k_y space is composed of the mixed xz and yz orbitals, but the electronic states along four lines are composed of pure xz or yz orbital. The same orbital components in two bands couple to open the SDW gap. The optical transition at the anti-node is from pure xz to pure xz or from pure yz to pure yz , while that at the Dirac node is from pure xz to pure yz or from pure yz to pure xz . The symmetry of the electronic transition at the anti-node is $A_{1g}+B_{2g}$ and that at the node is B_{1g} . The symmetry difference enables us to detect the anti-node and the node separately. The experimentally obtained B_{2g} spectra show critical fluctuation just above T_{SDW} and jump into the gap structure at T_{SDW} , while the B_{1g} spectra gradually change as temperature decreases through the T_{SDW} .^{49,50} The gap structure is composed of the reduced intensity below 300 cm^{-1} and the peaks at 400 and 800 cm^{-1} . The anti-nodal gap energies are the same as those in infrared spectroscopy⁵¹ and ARPES.^{52–57}

The magnetic exchange interaction energies also cannot be simply determined. The exchange interaction energies calculated in the superexchange interaction model are antiferromagnetic with the similar magnitude in the x and y directions, $J_{1x} \approx J_{1y}$, because the anisotropy between x and y is small even in the orthorhombic SDW structure.^{31,33} In order to stabilize the stripe spin structure, the next nearest neighbor exchange interaction energy J_2 must be larger than half of the nearest neighbor exchange interaction energy. On the other hand the exchange interaction energies obtained from the second derivative of the total energy of the stripe spin structure with respect to the angle of

the moments are antiferromagnetic in the x direction and weak ferromagnetic in the y direction.^{32,34} The superexchange interaction is related to the strong correlation of on-site Hubbard Coulomb repulsion. It was argued that the systems are moderately correlated and the largely local iron moments are driven by Hund's intra-atomic exchange rather than by the on-site Hubbard repulsion.¹⁶

The magnetic excitations observed by neutron scattering are analyzed (1) by the antiferromagnetic interactions in both x and y directions^{9,14,18,30,41,58} and (2) antiferromagnetic in x and ferromagnetic in y .^{14,59} Usually the full spin wave dispersion is obtained in the localized spin picture. The similar dispersion is also obtained in the itinerant spin picture, but the high-energy parts are decayed into particle-hole excitations (Stoner continuum) and the continuum excitations extend above the maximum of the spin wave dispersion.⁶⁰⁻⁶³ Many low-energy neutron scattering experiments did not reach the top of the dispersion.^{9,10,14,30,41,58} Diallo *et al.*¹⁸ observed broad magnetic dispersion above 100 meV and suggested the damping of spin waves by the particle-hole excitations, while Zhao *et al.*⁵⁹ reported the full spin wave dispersion expressed by the antiferromagnetic in x and ferromagnetic in y . No consensus is obtained whether the itinerant or localized view is appropriate at present.

In order to clarify whether the exchange interaction energies are determined by the short-range superexchange interaction mechanism or the total energy of the long-range stripe spin structure, the selection rule of two-magnon Raman scattering from the stripe spin structure was investigated. Two-magnon scattering in the insulating antiferromagnet is caused by the change of two spins $\Delta S^z = \pm 1$. We found that the two-magnon scattering mechanism can be separately considered for the change of spins at the nearest neighbor sites and the next nearest neighbor sites. They give different symmetries and peak energies. Applying this selection rule to the two-magnon Raman scattering, it is found that the exchange interaction are given by the total energy mechanism.

The peak energy of the present metallic magnetic Raman spectra is the same as the two-magnon scattering from localized spins in insulator, but the large spectral weight above twice the maximum energy of the spin wave dispersion cannot be understood by the two-magnon scattering process. Magnetic Raman spectra in metal is usually expressed by the two-magnon scattering from decayed spin waves. The decrease of the spin correlation length reduces the magnetic excitation energy as well as the life time. Therefore the large spectral weight at high energy cannot be interpreted by this model. We have to take into account the magnetic component of the itinerant carriers travelling

in the antiferromagnetic spin sea. The effect is interpreted both in the localized spin model and the itinerant spin model. In the localized spin model the high-energy magnetic scattering is interpreted as electronic scattering of itinerant carriers in the AF spin lattice, because the moving carriers overturn spins and the electron spectral function have the magnetic component expressed by the self-energy in the string model.⁶⁴⁻⁷¹ In the itinerant model the magnetic scattering is interpreted as particle-hole excitations from the majority spin states to the minority spin states.⁶⁰⁻⁶³ The magnetic scattering in metallic BaFe₂As₂ is compared to the hole-doped La_{2-x}Sr_xCuO₄ and electron-doped Nd_{2-x}Ce_xCuO₄. The electron density dependence in BaFe₂As₂ is found to be different from the cuprates

The present experiments are based on the theoretical findings that the electronic excitations near the Dirac node and the anti-node can be separately detected using the different Raman symmetries and the nearest and the next nearest neighbor exchange interaction energies can be also separately detected using the different Raman symmetries. Hence the relevant theories are presented followed by the experimental results. Section 2.1 presents the electronic Raman scattering mechanism of the SDW gap which is different from the normal metal and the superconducting gap. Section 2.2 presents the formulation of the nodal gap and anti-nodal gap in the two-orbital tight binding model. Section 2.3 presents the experimental procedure. Section 2.4 presents the experimental results of the high-energy spectra of the electronic Raman scattering and the magnetic Raman scattering. Section 2.5 presents the low-energy spectra of the Dirac node and the anti-node. Section 2.6 presents phonons. Section 3.1 presents the robust antiferromagnetic correlation in two-dimensional magnetism. Section 3.2 presents the symmetry of two-magnon scattering. Section 3.3 presents the experimental results of two-magnon Raman scattering. Section 3.4 presents the effect of conductive carriers to the magnetic scattering in comparison to the cuprate superconductors.

2. SDW State

2.1 Raman scattering of the SDW gap

Sometimes the SDW gap is treated in the similar way as the superconducting gap in the Raman scattering experiment. However, their excitation processes are completely different. The Raman scattering of the superconducting gap is expressed by the intra-band transition with the momentum shift $|\mathbf{k}_f - \mathbf{k}_i| = \Delta k \approx 0$ at $\mathbf{k}_i \approx \mathbf{k}_F$, where \mathbf{k}_F is the Fermi wave vector. On the other hand the SDW gap scattering is expressed by the

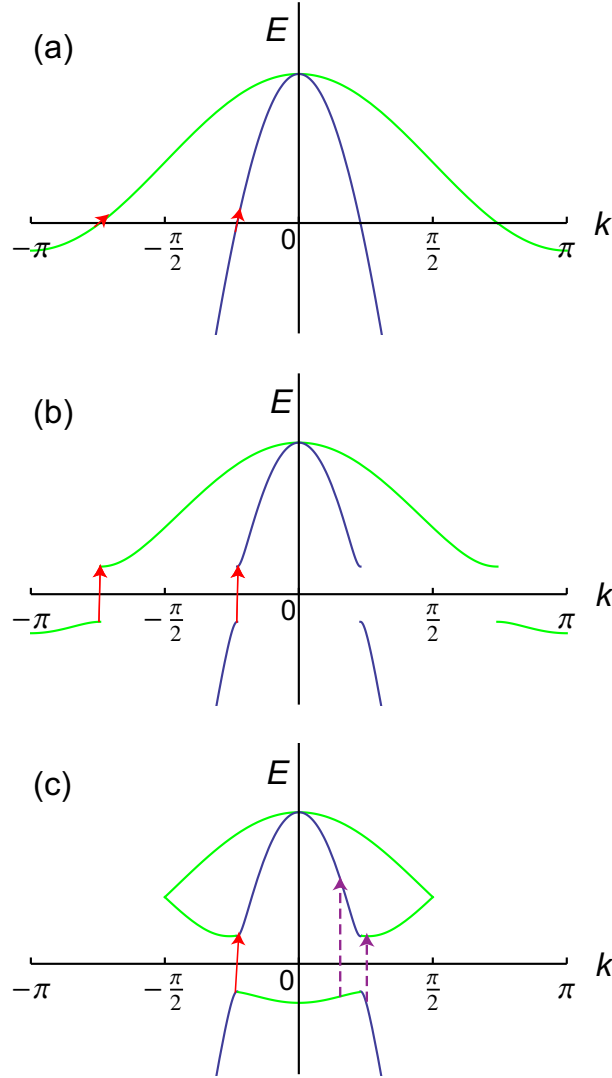


Fig. 1. (color online) (a) Intraband electronic Raman excitations (red arrows) in the normal state. The green band has the electron pocket at $k = \pi$ and the blue band has the hole pocket at $k = 0$. The momentum shift in the Raman process is kept to be small in order to satisfy the momentum conservation with incident and scattered light. (b) In the superconducting state the excitation across the gap gives the pair breaking spectra. The electronic transition is limited to near the original Fermi surface. The initial and the final states are on the same band. (c) In the SDW state the electronic bands are folded into $-\pi/2 \leq k \leq \pi/2$. The intraband electronic excitations are limited to near the band crossing parts, while the interband transitions (purple dashed arrows) are available anywhere. Therefore the interband transition is dominant.

interband transition between the original band and the folded band produced by the momentum shift of \mathbf{k}_{nest} , where \mathbf{k}_{nest} is the nesting vector $(\pi, 0)$. The vertical transition is allowed all over the folded Brillouin zone.

Electronic Raman scattering in the normal state is induced by the first order of the

\mathbf{A}^2 term and the second order of the $\mathbf{p} \cdot \mathbf{A}$ term in the electron-radiation interaction term $(\mathbf{P} - \frac{e}{c}\mathbf{A})^2$. The matrix element is^{72,73}

$$M = e_i^\alpha e_s^\beta \frac{1}{m} \left[\delta_{\alpha\beta} + \frac{1}{m} \left(\sum_t \frac{\langle c, \mathbf{k}_f | P_\beta | b, \mathbf{k}_i + \mathbf{q}_i \rangle \langle b, \mathbf{k}_i + \mathbf{q}_i | P_\alpha | a, \mathbf{k}_i \rangle}{\epsilon_{t, \mathbf{k} + \mathbf{q}_i} - \epsilon_{s, \mathbf{k}} - \omega_i} + X \right) \right], \quad (1)$$

where X is the term with the different time order, m the free electron mass, e_i^α and e_s^β polarization vectors of incident and scattered light, α and β the Cartesian coordinate, ω_i and \mathbf{q}_i the incident photon energy and wave vector, a , b , and c are the bands of the initial, intermediate, and final electronic states, and \mathbf{k}_i and \mathbf{k}_f are the initial and final wave vectors of the electron. The scattered photon wave vector \mathbf{q}_s is $\mathbf{k}_i + \mathbf{q}_i - \mathbf{k}_f$. The q_i and q_s are approximately zero.

If the electron returns to the initial band “*intraband transition*, $c = a$ ”, eq. (1) is the same form as the $\mathbf{k} \cdot \mathbf{p}$ perturbation. In the low energy and the long wavelength approximation of the incident light eq. (1) becomes

$$M = e_i^\alpha e_s^\beta \left(\frac{1}{m^*} \right)_{\alpha\beta}, \quad (2)$$

where $1/m^*$ is the effective inverse mass tensor at \mathbf{k}_i .

If the final band c is different from the initial band a “*interband transition*, $c \neq a$ ”, the scattering probability is determined by the symmetries of the initial and final electron wave functions.

Figure 1 shows the electronic Raman excitations in (a) the normal metal, (b) superconducting state, and (c) SDW state. In the normal state the momentum shift across the Fermi wave vector is the order of $\Delta k \lesssim k_{\text{ZB}}/1000$ to satisfy the momentum conservation with incident and scattered light, where k_{ZB} is the wave vector at the Brillouin zone boundary. The energy shift in Raman scattering from the intraband transition (red arrows) is usually limited to less than a few tens cm^{-1} , if the strong correlation effect is not taken into account. The scattering probability is expressed using the inverse mass tensor of eq. (2).

The electronic transition in the superconducting state is the *intraband transition*. The electronic excitation is limited to near the gap because of the momentum conservation with light. The scattering probability is expressed using the inverse mass tensor of eq. (2).^{11,74-76} The superconducting gap symmetry with the largest scattering intensity in $\text{BaFe}_{1.84}\text{Co}_{0.16}\text{As}_2$ is B_{2g} .^{11,50,77} The scattering intensities from the electron pockets and hole pockets were calculated using the inverse mass tensors and the screening terms

in two-band model¹¹ and the full-potential linearized augmented plane wave (LAPW) model.⁷⁶ The importance of the multi-orbital was pointed^{11,78,79}

In the SDW state the electronic bands are folded into $-\pi/2 \leq k \leq \pi/2$ for the nesting vector $\mathbf{k}_{\text{nest}} = (\pi, 0)$. The *intra*band transition is limited to near the gap as in the superconducting gap. However, the dominant electronic excitations are the *inter*band transition (purple dashed arrows) between the original band and the folded band all over the folded Brillouin zone. Among them the transitions at the rather wide area near the gap make the gap structure. The Raman intensity of the SDW gap is one hundred times larger than that of the superconducting gap. The electronic Raman scattering of the *inter*band transition is not given by the inverse mass tensor. The symmetries of the wave functions directly result in the scattering probability. Then we have to know the nested band structure to understand the Raman scattering of the SDW gap.

2.2 SDW state in the two-band model

The electronic states near the Fermi energy is created from the two-dimensional FeAs layer. Wang *et al.*²⁶ and Ran *et al.*²⁷ pointed out that the SDW gap in BaFe₂As₂ is not a full gap, but a nodal gap. In the two-orbital band model the hole pocket changes the dominant orbitals xz - yz - xz - yz on circling the Fermi surface, while the electron Fermi surface is represented by only one orbital. Under the conditions of (1) the collinear SDW order (denoted by the magnetization direction of x), (2) the inversion symmetry, and (3) the time-reversal symmetry, the vorticity is ± 2 for the hole pockets and 0 for the electron pockets. It creates the Dirac nodes with the vorticity ± 1 in the SDW gap. The nodes are located at the intersection between the SDW wave vector and the hole Fermi surface in the two-band model. The Dirac nodes are shown to be stable in the five band model, too.^{27,29}

The different optical selection rule near the node and the anti-node is expressed by the two-orbital model of xz and yz . Using the transfer integrals by Qi *et al.*⁴² and Raghu *et al.*⁴³ the tight-binding Hamiltonian is

$$H_0 = \sum_{\mathbf{k}, \sigma} (d_{xz, \sigma}^\dagger(\mathbf{k}), d_{yz, \sigma}^\dagger(\mathbf{k})) \mathbf{K}(\mathbf{k}) \begin{pmatrix} d_{xz, \sigma}(\mathbf{k}) \\ d_{yz, \sigma}(\mathbf{k}) \end{pmatrix}, \quad (3)$$

where 2×2 matrix $\mathbf{K}(\mathbf{k})$ is

$$\begin{aligned} \mathbf{K}(\mathbf{k}) &= (\epsilon_+(\mathbf{k}) - \mu)\tau_0 + \epsilon_{xy}(\mathbf{k})\tau_1 + \epsilon_-(\mathbf{k})\tau_3, \\ \epsilon_+(\mathbf{k}) &= -(t_1 + t_2)(\cos k_x + \cos k_y) - 4t_3 \cos k_x \cos k_y, \end{aligned}$$

$$\begin{aligned}\epsilon_-(\mathbf{k}) &= -(t_1 - t_2)(\cos k_x - \cos k_y), \\ \epsilon_{xy}(\mathbf{k}) &= -4t_4 \sin k_x \sin k_y,\end{aligned}\tag{4}$$

where $d_{xz,\sigma}^\dagger$ and $d_{xz,\sigma}$ are the creation and annihilation operators of a d electron with the xz orbital and spin σ , μ the chemical potential, τ_i are Pauli matrices, and τ_0 is the unit matrix. t_1 is the transfer integral between xz orbitals and t_2 between yz orbitals at the nearest neighbor sites in the x direction. t_3 is the transfer integral between xz orbitals and t_4 between xz and yz orbitals at the diagonal sites. The band dispersions are given by

$$E_{\pm}(\mathbf{k}) = \epsilon_+(\mathbf{k}) \pm \sqrt{\epsilon_-^2(\mathbf{k}) + \epsilon_{xy}^2(\mathbf{k})} - \mu.\tag{5}$$

The upper and lower bands are called the electron band and the hole band, because they make the electron pockets and the hole pockets, respectively. The eigen functions are

$$\begin{aligned}\Psi_{\pm,\sigma}(\mathbf{k}) &= \frac{\epsilon_{xy}(\mathbf{k})}{A_{\mp}} d_{xz,\sigma} \\ &+ \frac{-\epsilon_-(\mathbf{k}) \pm \sqrt{\epsilon_-^2(\mathbf{k}) + \epsilon_{xy}^2(\mathbf{k})}}{A_{\mp}} d_{yz,\sigma},\end{aligned}\tag{6}$$

where the normalization factors A_{\pm} are

$$A_{\pm} = \sqrt{2 \left[\epsilon_{xy}^2(\mathbf{k}) + \epsilon_-^2(\mathbf{k}) \pm \epsilon_-(\mathbf{k}) \sqrt{\epsilon_-^2(\mathbf{k}) + \epsilon_{xy}^2(\mathbf{k})} \right]}.\tag{7}$$

The xz and yz components on the electron and hole bands are given by eq. (6).

Figure 2(a) shows the Fermi surfaces of hole pockets α and β and electron pockets γ and δ in the Brillouin zone of one Fe atom per unit cell. The transfer integrals are $t_1 = -1$, $t_2 = 1.3$, $t_3 = t_4 = -0.85$ in the unit of $|t_1|$.⁴³ The gray arrows are unit vectors in the direction of $(-\epsilon_{xy}(\mathbf{k}), \epsilon_-(\mathbf{k}))$, where $\epsilon_{xy}(\mathbf{k})$ represents the mixing between xz and yz orbitals and $\epsilon_-(\mathbf{k})$ represents the difference of xz and yz component.^{42-44,85} The upward component of the gray arrow is the xz component (red) and the downward component is the yz component (green) for the electron band and opposite for the hole band. The hole Fermi surface is composed of two orbitals whose weights gradually change on going round the Fermi surface. The Fermi surfaces in the k_x and k_y directions from $(0, 0)$ are composed of the pure xz and yz orbitals, respectively. The SDW state is formed by

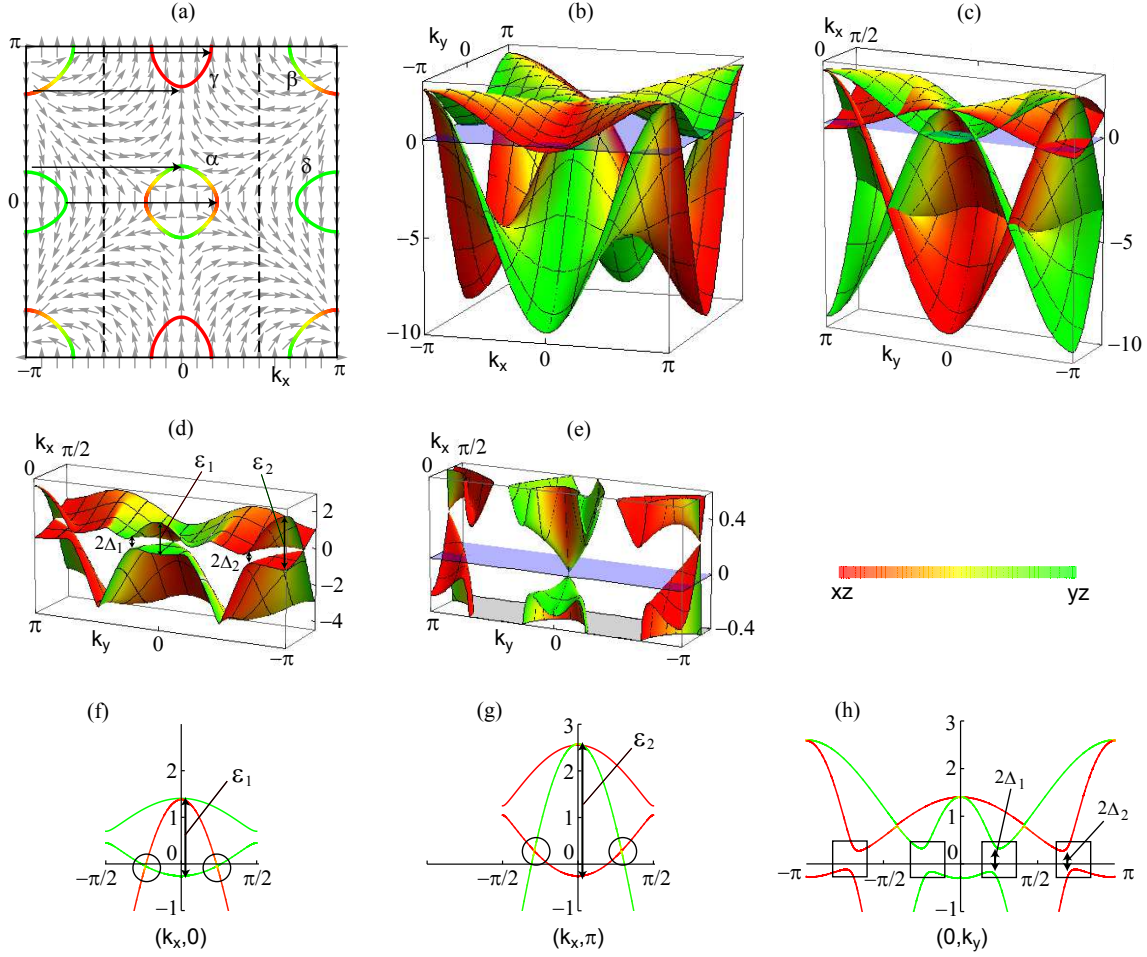


Fig. 2. (color online) (a) Hole Fermi surfaces α and β and electron Fermi surfaces γ and δ . The xz and yz orbital components are shown by red and green according to the color scale. The gray arrows indicate the unit vectors parallel to $(-\epsilon_{xy}(\mathbf{k}), \epsilon_{-}(\mathbf{k}))$.^{42, 43} The dashed lines show the unit cell in the SDW state. (b) Dispersions of the electron and hole bands. The E_F is shown by the translucent blue plane. (c) Folded bands in the SDW state. (d) Nodal gapped bands near the E_F . The uppermost dispersion is removed. (e) The same as above in the expanded energy scale. Note that the front side is $E - k_x$ in (b), while $E - k_y$ in (c)-(e). (f)-(h) Dispersions in $(k_x, 0)$, (k_x, π) , and $(0, k_y)$. The circle denotes the Dirac node and the square denotes the anti-node.

shifting the Brillouin zone by $\mathbf{k}_{\text{nest}} = (\pi, 0)$. The reduced zone into $-\pi/2 \leq k_x \leq \pi/2$ is shown by the dashed lines. Figure 2(b) shows the dispersions of the electron band and the hole band. The unit of the energy is $|t_1|$. The weight of the xz and yz orbitals are represented by the scale from red to green. The translucent blue plane shows the E_F . Figure 2(c) shows the dispersion in a half of the folded Brillouin zone without the band mixing. The crossing parts may split by the mixing. Note that the front side of the cross section is the $E - k_y$.

The local interaction to form the SDW with the wave vector $(\pi, 0)$ is²⁷

$$H_{\text{SDW}} = M_{ab} \sum_i (-1)^{i_x} (d_{i,a\uparrow}^\dagger d_{i,b\uparrow} - d_{i,a\downarrow}^\dagger d_{i,b\downarrow}), \quad (8)$$

where

$$M_{ab} = [\phi_0 \tau_0 + \phi_1 \tau_1 + \phi_2 \tau_2 + \phi_3 \tau_3]_{st}, \quad (9)$$

and a and b are orbitals and i_x is the x coordinate of the iron atomic site i in the unit of the inter-iron atomic distance. The $(-1)^{i_x}$ term gives the twofold periodicity in the x direction. ϕ_i is the mean field parameter to minimize the free energy including the correlation term. If the intra-orbital interaction τ_0 or τ_3 is dominant, the Dirac node appears at $k_y = 0$ and π which are the same as the calculations by Ran *et al.*,²⁷ Morinari *et al.*,²⁹ and Kaneshita *et al.*^{62,84}

Figures 2(d) and 2(e) show the gapped two bands near the E_F . The same orbital components in two bands couple to open a gap, if the τ_0 or τ_3 is dominant. The difference is scarcely found whether τ_0 or τ_3 is dominant. The connecting point of two Dirac cones is a little below E_F near $(0, 0)$ and above E_F near $(0, \pi)$, which causes small electron Fermi surfaces near $(0, 0)$ and hole Fermi surfaces near $(0, \pi)$. The electronic transitions near the Dirac nodes appear at the energy near zero and those at the anti-node appear at $2\Delta_1$ and $2\Delta_2$. The gap energies are $2\Delta_1 = 0.49$ and $2\Delta_2 = 0.39$, when the coupling constant $\phi_0 = 0.3$ or $\phi_3 = 0.3$ in the energy unit of $|t_1|$. The transitions near the Dirac node and anti-node have different symmetries, because the former is the transition between yz and xz while the latter between yz and yz near $(0, 0)$ or xz and xz near $(\pi, 0)$. The $\Delta k \approx 0$ transition ϵ_1 from yz to $xz + yz$ at $(0, 0)$ and ϵ_2 from xz to $xz + yz$ at $(0, \pi)$ in Fig. 2(d) have large joint density of states. The energies are not strongly affected by the coupling term eq. (9). The dispersions in $(k_x, 0)$, (k_x, π) , and $(0, k_y)$ are shown in Figs. 2(f)-(h).

2.3 Experimental Procedure

Single crystals of BaFe_2As_2 were grown by the self-flux method. Raman spectra were measured on the fresh cleaved surfaces in a quasi-back scattering configuration using 5145 Å laser light. The polarization configuration of the Raman spectra is presented by $(e_i e_s)$. The crystallographic axes of the tetragonal structure are a and b . The bisecting directions are x and y . The x and y directions are rotated by 45° from the a and b . The observed Raman spectra include phononic, magnetic, and electronic excitations. Raman

active phonon modes are $1A_{1g} + 1B_{1g} + 2E_g$ in the tetragonal structure.^{80–83} The orthorhombic structure ($Fmmm$) is the sub-group of the tetragonal structure ($I4/mmm$). The second order phase transition is allowed from the change of the symmetry, but whether the transition is the first order or the second order is determined by the free energy. It is known that the transition becomes the first order, if the SDW transition is accompanied by the structural phase transition. In the present case the first order transition of BaFe_2As_2 has been confirmed in many experiments.^{9,17,35–39} The (aa) spectra allow the $A_{1g} + B_{1g}$ ($A_g + B_{1g}$) modes, (ab) B_{2g} (A_g) mode, (xx) $A_{1g} + B_{2g}$ (A_g), and (xy) B_{1g} (B_{1g}) in the tetragonal (orthorhombic) structure. The Raman system was calibrated using a black body radiation so that the intensity is proportional to the Raman probability independently to the scattered light wave number.

2.4 High-energy spectra of the anti-nodal gaps and the transitions at $(0, 0)$ and $(0, \pi)$ points

Figure 3 shows the temperature dependence of polarized Raman spectra. The sharp peaks at 181 and 215 cm^{-1} are caused by the A_{1g} and B_{1g} phonons, respectively. The broad hump with the top energy 2400 \sim 2500 cm^{-1} at 300 K is the two-magnon scattering peak. The two-magnon intensity increases with decreasing temperature. Below $T_{\text{SDW}} \approx 130$ K new peaks appear at 400, 800, 2150, and 3500 cm^{-1} .

As stated in § 2.1 the electronic scattering in the normal phase is limited to less than a few tens cm^{-1} . The wide-energy intensity is derived from only magnetic excitations. In order to estimate the interband transition activated by the SDW transition, the differential spectra between the SDW state at 10 K and the normal state at 200 K are shown in Fig. 4(a). The intensity scales are the same for different polarization configurations. It is noted that the differential spectra include the electronic scattering component which is activated in the SDW state and the two-magnon scattering component whose intensity increases with decreasing temperature. In order to clearly show the magnetic scattering component, the scattering intensities in the normal states at 200 K and 300 K are enlarged to the estimated level at 10 K in Fig. 4 (b). The zero levels are adjusted. The spectra at 200 K and 300 K are almost the same. It confirms that the spectral shape of the magnetic scattering is the same except the intensity in the normal phase. The extra humps appeared at 10 K are created by the interband electronic transitions. The differential spectra between 10 K and 200 K are shown by the black curve. The peak positions are shown by the arrows. The 800 and 400 cm^{-1}

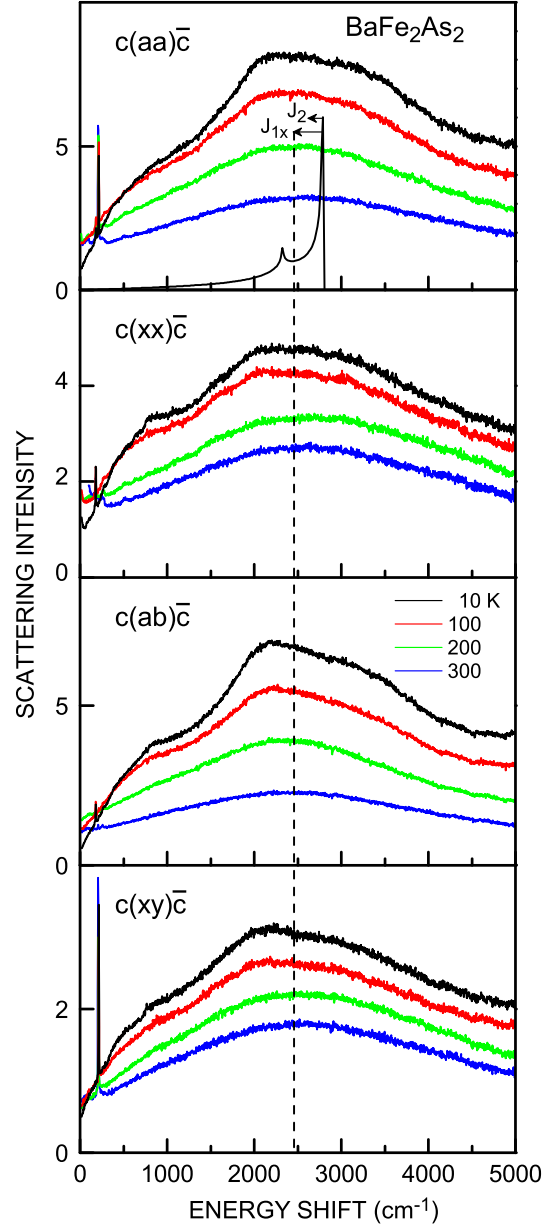


Fig. 3. (color online) Temperature dependence of polarized Raman spectra in BaFe_2As_2 .

peaks are assigned to the anti-nodal SDW gaps of $2\Delta_1$ and $2\Delta_2$ and the 2150 and 3500 cm^{-1} peaks to the transitions ϵ_1 at $(0, 0)$ and ϵ_2 at $(0, \pi)$ points as shown in Figs. 2(d), 2(f), and 2(g). These peak intensities are large in (aa) , (ab) , and (xx) and small in (xy) . The $2\Delta_1$ and $2\Delta_2$ are the transition from yz to yz and from xz to xz , respectively. The ϵ_1 is the transition from yz to yz and xz . The density of the final state is larger in yz than xz . The ϵ_2 is the transition from xz to xz and yz . The density of the final state is larger in xz than yz . The symmetry of the transitions from xz to xz and from yz to yz

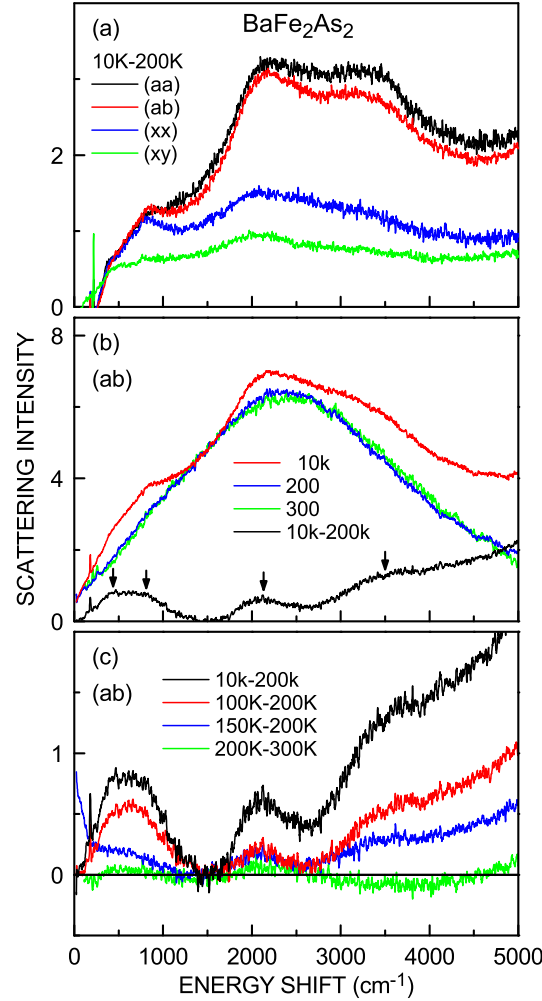


Fig. 4. (color online) (a) Differential Raman spectra between the SDW state at 10 K and the normal state at 200 K. (b) The Raman spectra at 10 K in the SDW phase and at 200 and 300 K in the normal phase. The 10 K spectra include electronic scattering activated by the Brillouin zone folding and magnetic scattering. The 200 and 300 K spectra is only magnetic scattering above a few tens cm⁻¹. The spectra at 200 K and 300 K are expanded in intensity and the zero levels are adjusted. The differential spectra between 10 K and 200 K are shown by the black curve. (c) Differential spectra obtained in the same way as (b).

is $A_{1g} + B_{2g}$ and that from xz to yz is B_{1g} . The (aa) , (xx) , (ab) , and (xy) spectra are active in $A_{1g} + B_{1g}$, $A_{1g} + B_{2g}$, B_{2g} , and B_{1g} , respectively. Therefore the (xx) , (ab) , and (aa) spectra observe above four transitions strongly and (xy) spectra observe ϵ_1 and ϵ_2 weakly. The experimental results roughly satisfy the selection rule.

Figure 4(c) shows the differential spectra between the SDW phase and the normal phase at 200 K, and also between 200 K and 300 K in the normal phase. The 400, 800, 2150, and 3500 cm⁻¹ peaks start to increase below the T_{SDW} . The peaks are observed

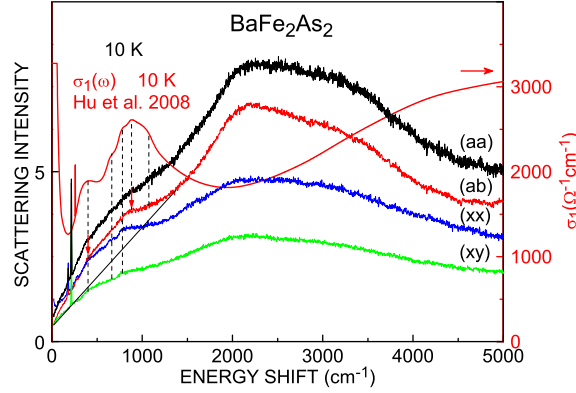


Fig. 5. (color online) Comparison between the Raman spectra and the optical conductivity spectra⁵¹ in the SDW state.

at 150 K which is a little above $T_{\text{SDW}} \approx 130$ K of this sample. The intensities of these peaks increase like the second order transition as temperature decreases.

Figure 5 shows the 10 K spectra at various polarization configurations and the optical conductivity at 10 K obtained by Hu *et al.*⁵¹ The 400 and 800 cm^{-1} SDW gap peaks in the present Raman spectra correspond to the 360, 890 cm^{-1} peaks in the optical conductivity.⁵¹ They are also correspond to the gaps observed in ARPES.⁴⁷ The fine peaks are noticeable in Raman and infrared spectra. The 662 and 780 cm^{-1} peaks in the (xx) and (xy) spectra and the 882 and 1072 cm^{-1} peaks in the (aa) and (ab) spectra correspond to the fine structure in the optical conductivity spectra.⁵¹ There are two possibilities for the origin of the fine structure. One is the electronic transition and the other is the phonon side band. Many other transitions may appear in the five band model.^{27,84} Yi *et al.*⁵⁶ reported in ARPES that the electronic structures are reconstructed in the SDW state and may not be described in the simple folding scenario by the correlation effect, because the introduction of Hubbard U in the local-density approximation to fit the band dispersion changes the structure at E_{F} . The continuum between 400 and 800 cm^{-1} may have such effects. The Fermi surfaces have rather large three-dimensional characters⁸⁵ and it may induce some complicated structure. On the other hand the energy difference 118 cm^{-1} and 190 cm^{-1} between the main peak and the fine peak is close to the 117 cm^{-1} E_{g} phonon energy and the 182 cm^{-1} $A_{1\text{g}}$ phonon energy.⁸¹ Those phonon modes forming the phonon side bands may be localized modes.⁸⁶

The humps at 2150 and 3500 cm^{-1} are not observed in the infrared spectra, because the d - d transition is infrared inactive. We assigned the humps to the ϵ_1 and ϵ_2 transitions

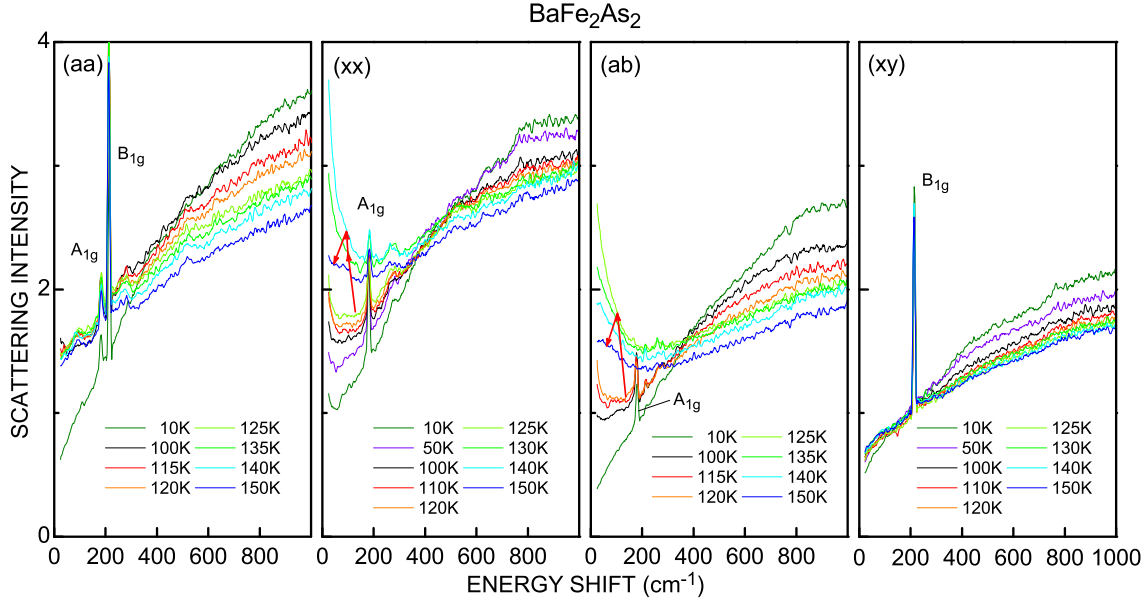


Fig. 6. (color online) Temperature dependent low-energy Raman spectra in BaFe_2As_2 . The low-energy spectra below 300 cm^{-1} jump to the high-intensity level at T_{SDW} and then gradually decreases as temperature increases in the (xx) and (ab) spectra. The red arrows show the jumps. The (aa) and (xy) spectra do not show the jump.

in Fig. 2(d). Those transitions may be related to the flat bands whose energies decrease with the increase of U . The U reduces the magnetic moment $M = 0.5 \sim 1 \mu_{\text{B}}/\text{Fe}$ in the local-density approximation plus Hubbard U (LDA+ U) band calculation.⁵⁶ However, it is difficult to compare the Raman peaks to the band calculation, because the bandwidth is renormalized and the energy shift is different at the Γ and X points to fit the ARPES data.

2.5 Low-energy spectra of the Dirac node and the anti-node

The temperature dependence of the polarized low-energy Raman spectra is shown in Fig. 6. All the spectra are plotted in the same intensity scale. The sharp peaks at 181 and 215 cm^{-1} are the A_{1g} and B_{1g} phonons in the tetragonal phase, respectively. They are discussed later. The 400 and 800 cm^{-1} humps are observed at 10 K in all polarization configurations. However, the temperature dependence below 300 cm^{-1} is very different between the (aa) and (xy) group and the (xx) and (ab) group. In the (xx) and (ab) spectra the low-energy scattering intensity abruptly increases from 125 K to 130 K in the (xx) spectra and from 120 K to 125 K in the (ab) spectra, and then gradually decreases as temperature increases.^{49,50} On the other hand the jump is not

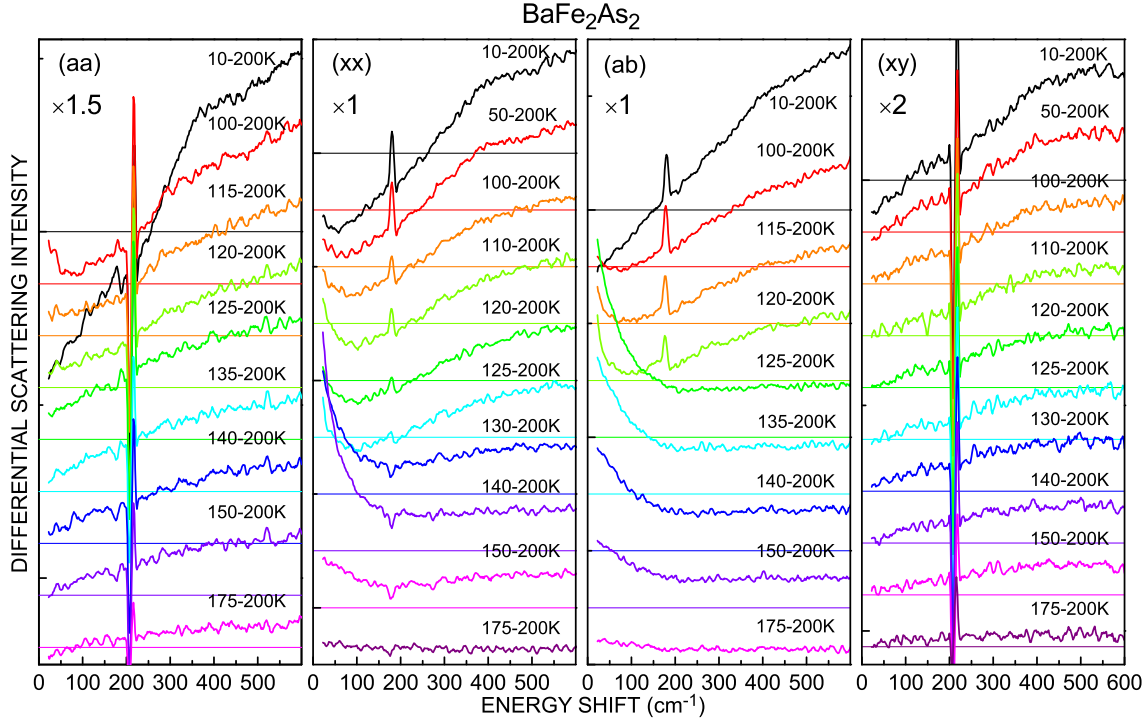


Fig. 7. (color online) Differential spectra from 200 K. The intensity below 200 cm^{-1} increases in the (xx) and (ab) spectra as temperature decreases below 150 K and jumps to the low intensity at T_{SDW} . The SDW-induced anti-nodal gap peaks at 400 and 800 cm^{-1} gradually increase in intensity as temperature decreases below a little above T_{SDW} in all polarization configurations, but is weakest in (xy) . The zero levels are shown by the same color lines.

observed in the (aa) and (xy) spectra near the T_{SDW} . The small temperature difference of the jump in (xx) and (ab) is induced by the first order transition.

It is noted that the experiment was made in the sequence of (aa) and (ab) at 10 K, (aa) and (ab) at 100K, \dots , 300 K and after rotating the sample by 45° (xx) and (xy) at 10 K, (xx) and (xy) at 50 K, \dots , 300 K. The (aa) and (ab) spectra at the same temperature are obtained exactly in the same condition except for the scattered light polarization. The same is for (xx) and (xy) . Therefore the spectral jump at T_{SDW} in the (xx) and (ab) spectra and the continuous change in the (aa) and (xy) spectra are intrinsic properties of this material.

Figure 7 shows the differential Raman spectra between various temperatures and 200 K. The zero levels are shown by the horizontal lines with the same color as the spectra. In the (xx) and (ab) spectra the intensity below about 200 cm^{-1} increases with decreasing temperature from 150 K to $T_{\text{SDW}} \approx 130 \text{ K}$ and then jumps to decrease by the opening of the SDW gap. On the other hand the jump is not observed in the (aa)

and (xy) spectra.

The above difference between the (xx) and (ab) group and the (aa) and (xy) group is caused by the different symmetries for the electronic transitions near the anti-node and the Dirac node. The electronic transition near the anti-node is from xz to xz or from yz to yz and that near the Dirac node is from xz to yz or from yz to xz . The symmetry of the transition near the anti-node is $A_{1g} + B_{2g}$ and that near the node is B_{1g} . The (xx) spectra are active to $A_{1g} + B_{2g}$ and (ab) to B_{2g} , (aa) to $A_{1g} + B_{1g}$, and the (xy) to B_{1g} . Therefore the (xx) and (ab) spectra represent the electronic transitions near the anti-node and the (aa) and (xy) spectra represent the Dirac node, if the A_{1g} component from the anti-node is ignored. The spectra representing the anti-node have the jump into the gap spectra. On the other hand the spectra representing the Dirac node has not the specific change at T_{SDW} . The A_{1g} component might be observed in the (aa) spectra, but the spectra do not show the jump at T_{SDW} . Instead the (aa) spectra gradually change into the spectra of the gapped excitations. In contrast to the (aa) spectra the gap spectra are weak in the (xy) spectra which represents only the excitation near the node.

The increase of the low-energy scattering intensity on approaching the T_{SDW} from high temperature is induced by the critical fluctuation relating to the opening of the anti-nodal gap, because it is observed only in the B_{2g} symmetry in which the anti-nodal gap excitations are observed. The magnetic fluctuation above T_{SDW} was also observed in neutron scattering.¹⁰ The critical fluctuation is the characteristic properties of the second order phase transition. The simultaneous SDW and structural transitions in BaFe_2As_2 splits into two second-order-like transitions on substituting Co for Fe.³⁶ The phase locking of the SDW to the lattice potential by the simultaneous structural transition changes the transition into the first order and the SDW into the commensurate one. The SDW and structural phase transition of BaFe_2As_2 is, however, close to the second order transition. It induces the critical fluctuation.

The above analysis is done on the assumption that the dominant orbital mixing term is τ_0 or τ_3 in eq. (9). If τ_1 or τ_2 is dominant, the positions of the Dirac node and the anti-node are exchanged and the observed spectral symmetries at the T_{SDW} become inconsistent to those of the electronic transitions.

As discussed above the symmetry dependence of the observed spectra is consistently interpreted by the electronic excitations near the anti-node and the Dirac node. However, the dominant orbitals at the nesting parts in electron pocket may be modified in

the five band model.^{20,44,45,85,87,88} More detailed theoretical analysis is expected.

2.6 Phonon mode activated in the SDW state

The sharp peaks in the tetragonal phase above T_{SDW} are observed at 181 (A_{1g}) cm^{-1} in the (aa) and (xx) spectra and 215 cm^{-1} (B_{1g}) in the (aa) and (xy) spectra of Fig. 6.⁸⁰⁻⁸³ Below T_{SDW} the (A_{1g}) peak appears at 187 cm^{-1} in the (ab) spectra. The A_{1g} mode in the tetragonal ($I4/mmm$) structure changes into the A_g mode in the orthorhombic structure by the compatibility relation of the group theory. Taking into account the 45° rotation of the crystallographic axes at the phase transition from the tetragonal to the orthorhombic structure, the Raman intensity of the A_g mode in the (ab) (in the tetragonal notation) polarization configuration is proportional to $|R_{11} - R_{22}|^2$ using the Raman tensor in the orthorhombic structure. The intensities in the (aa), (xx), and (yy) spectra are proportional to $\frac{1}{4}|R_{11} + R_{22}|^2$, $|R_{11}|^2$, and $|R_{22}|^2$, respectively. The (xx) and (yy) spectra may mix if the crystal is twinned, but both spectra represents the same A_g mode and the difference is small even in the untwinned crystal. Other polarization configurations are not affected by the twin structure. The intensities in the (aa), (xx), and (yy) spectra are expected to be nearly the same and much larger than that in the (ab) spectra because $R_{11} \approx R_{22}$. Instead at 10 K the intensities in the (xx) and (ab) spectra are $1.5 \sim 2$ times as large as the intensity in (aa). This phonon is the mode in which As atom moves in the c direction.⁸⁰ It has large magneto-phonon interaction, because the Fe-As-Fe angle is very sensitive to the Fe-Fe exchange interaction energy.^{31,32,89} The detailed mechanism of the enhancement is still an open question. The enhancement of the A_{1g} phonon below T_{SDW} was reported in CaFe_2As_2 ⁸² and $\text{BaFe}_{2-x}\text{Co}_x\text{As}_2$.⁸³ Similar enhancement of the infrared active phonon was reported in BaFe_2As_2 ⁹⁰

3. Magnetic Raman Scattering

3.1 Antiferromagnetic correlation in low-dimensional magnetism

The exchange interaction energies are very different whether the calculation starts from the short-range superexchange interaction or from the total energy of long-range AF stripe spin structure. In the former case the calculation of the local superexchange interaction gives AF exchange interaction energies for all directions reflecting the equivalent x and y directions. The stripe spin order is stable if $J_{1x} = J_{1y} < 2J_2$, otherwise the checkerboard spin order is stable.^{31,33} On the other hand in the latter case the

exchange interaction energies are obtained from $J_{ij}(R) = -\partial^2 E / \partial \theta_i(0) \partial \theta_j(R)$, where E is the total energy and $\theta_j(R)$ is the angle of the moment of the j th spin.^{32,34} The calculated energies are antiferromagnetic $SJ_{1x} = 43$, ferromagnetic $SJ_{1y} = -3.1$, and antiferromagnetic diagonal $SJ_2 = 14.3$ meV.³⁴ The low-energy spin wave in the SDW state was observed by neutron scattering in BaFe_2As_2 ,^{10,14} SrFe_2As_2 ³⁰ and CaFe_2As_2 .⁴¹ Ewings *et al.*¹⁴ fitted the spin wave velocity at 7 K in BaFe_2As_2 by (1) the long-range exchange interaction model with $SJ_{1x} = 36$, $SJ_{1y} = -7.2$, and $SJ_2 = 18$ meV and (2) the short-range exchange interaction model with $SJ_{1x} = 17.5$, $SJ_{1y} = 17.5$, and $SJ_2 = 35$ meV. Zhao *et al.* disclosed in high-energy neutron scattering that the entire spin wave dispersion of CaFe_2As_2 ($T_N \approx 170$ K) at 10 K is expressed by the long-range model with $SJ_{1x} = 49.9$, $SJ_{1y} = -5.7$, $SJ_2 = 18.9$, and $SJ_z = 5.3$ meV.⁵⁹

The spin wave dispersion ignoring the anisotropy terms is given by¹⁴

$$\hbar\omega(k) = \sqrt{A^2 - D^2}, \quad (10)$$

$$A = 2S \left\{ J_{1y} \left[\cos \frac{k_y}{2} - 1 \right] + J_{1x} + 2J_2 + J_z \right\}, \quad (11)$$

$$D = 2S \left\{ J_{1x} \cos \frac{k_x}{2} + 2J_2 \cos \frac{k_x}{2} \cos \frac{k_y}{2} + J_z \cos k_z \right\}. \quad (12)$$

Figure 8 shows the dispersion at $k_z = 0$ with (a) $SJ_{1x} = 36$, $SJ_{1y} = -7.2$, $SJ_2 = 18$,¹⁴ and $SJ_z = 5.3$ meV, (b) $SJ_{1x} = 17.5$, $SJ_{1y} = 17.5$, $SJ_2 = 35$,¹⁴ and $SJ_z = 5.3$ meV, and (c) $SJ_{1x} = 40$, $SJ_{1y} = 40$, $SJ_2 = 20$, and $SJ_z = 5.3$ meV. (a) and (b) have nearly the same spin wave velocity, but the maximum energy in (b) is lower than in (a). The energy at $k_x = 0$ or $k_y = 0$ goes to zero at the critical point of (c) $J_{1x} = J_{1y} = 2J_2$ in Fig. 8(c).

The superconducting phase does not overlap the SDW phase or slightly overlaps at the crossover region, if it is observed by quasi-static experiments such as magnetic susceptibility, resistivity, specific heat, μSR , and crystal structure.^{36,91-93} Sometimes it is called as the evidence of competing superconductivity and magnetism. However, such a phase diagram is valid only at $k \approx 0$ and $\omega \approx 0$. Neutron scattering experiments in high temperature superconductors disclosed that only the magnetic correlation perpendicular to the CuO_2 plane disappears above the magnetic transition temperature.⁸⁻¹⁰ This is a common property in low dimensional magnetism. The AF transition temperature T_N in two-dimensional antiferromagnet is determined by the weakest exchange interaction

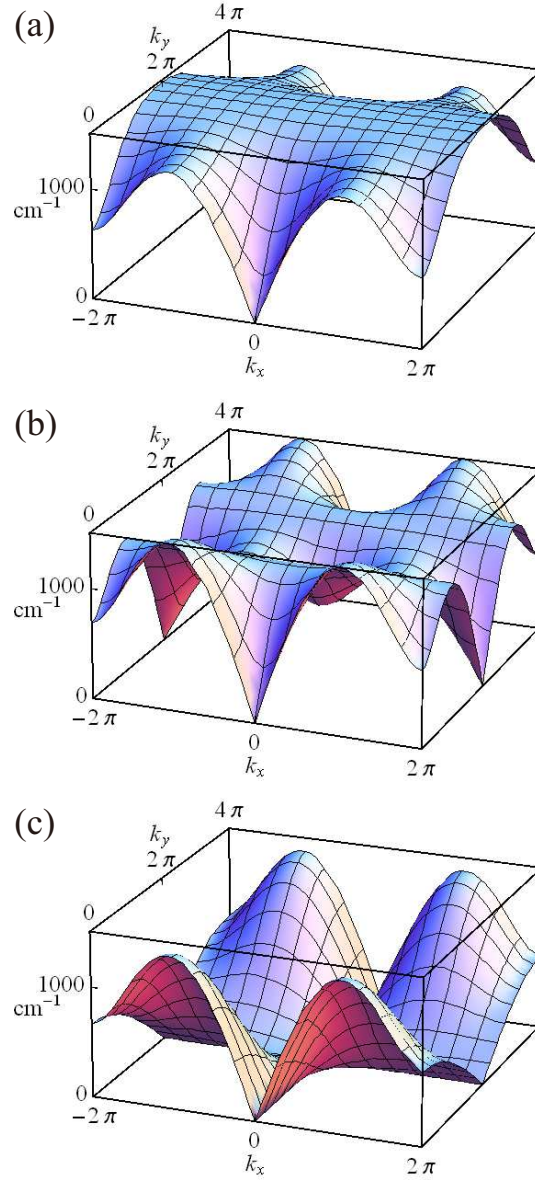


Fig. 8. (color online) Spin wave dispersion at $k_z = 0$ with (a) $SJ_{1x} = 36$, $SJ_{1y} = -7.2$, $SJ_2 = 18$,¹⁴ and $SJ_z = 5.3$ meV, (b) $SJ_{1x} = 17.5$, $SJ_{1y} = 17.5$, $SJ_2 = 35$,¹⁴ and $SJ_z = 5.3$ meV, and (c) $SJ_{1x} = 40$, $SJ_{1y} = 40$, $SJ_2 = 20$, and $SJ_z = 5.3$ meV.

J_z as⁷

$$T_N = J_z \left(\frac{L}{d} \right)^2, \quad (13)$$

where L is the intralayer AF spin correlation length and d is the inter-spin length in the layer. Neutron scattering showed that the correlation length is $15 \sim 18$ Å at 136 K ($\sim T_{\text{SDW}}$) and it remains to be $6 \sim 8$ Å at 180 K.^{9,10} The magnetic excitations with the wavelength longer than the correlation length may disappear but those with

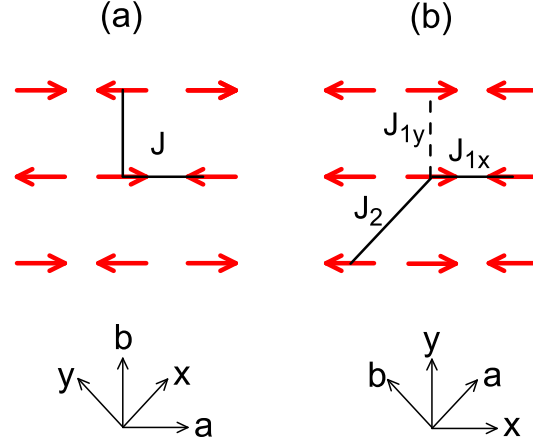


Fig. 9. (color online) Spin structures in (a) the checkerboard type in the cuprate superconductors and (b) the stripe type in BaFe_2As_2 . The AF exchange interactions are presented by the line segments and the ferromagnetic interaction by the dashed line segment. Note that a and b are the tetragonal crystallographic axes at high temperatures.

shorter wavelength survive above T_N and even in the superconducting phase. Two-magnon Raman scattering in the AF insulator represents the joint density of states of k and $-k$ magnons to satisfy the momentum conservation with light. The dominant part is derived from the zone boundary with the large density of states. Therefore the two-magnon peak survives till the last as the correlation length decreases.

3.2 Symmetry of two-magnon scattering induced by Coulomb interaction in insulator

Two-magnon scattering in AF insulator arises from the simultaneous changes of $\Delta S_z = \pm 1$ on both spin sublattices by the Coulomb interaction.^{94–99} The two-magnon Hamiltonian can be written as⁹⁵

$$H_{\text{two-mag}} = \sum_{\substack{\mathbf{R}\mathbf{r} \\ \alpha\beta\gamma\delta}} B_{\alpha\beta\gamma\delta}(\mathbf{r}) e_i^\alpha e_s^\beta S_{\mathbf{R}}^\gamma S_{\mathbf{R}+\mathbf{r}}^\delta, \quad (14)$$

where e_i and e_s are incident and scattered light polarizations and \mathbf{r} is the vector from the site \mathbf{R} to the antiparallel spin site. B is determined so that $H_{\text{two-mag}}$ is totally symmetric. The spin term $S_{\mathbf{R}}^\gamma S_{\mathbf{R}+\mathbf{r}}^\delta$ is taken so that the total z component of excited spins is zero as

$$S_{\mathbf{R}}^x S_{\mathbf{R}+\mathbf{r}}^x + S_{\mathbf{R}}^y S_{\mathbf{R}+\mathbf{r}}^y = \frac{1}{2} (S_{\mathbf{R}}^+ S_{\mathbf{R}+\mathbf{r}}^- + S_{\mathbf{R}}^- S_{\mathbf{R}+\mathbf{r}}^+). \quad (15)$$

In order to clarify the difference in the selection rule of the stripe AF spin structure in BaFe_2As_2 and the checkerboard AF spin structure in cuprate superconductors, the

checkerboard-type is first discussed. The spin structure is shown in Fig. 9(a). The nearest neighbor spins are in the a and b directions. All the nearest neighbor spins are antiparallel. The next nearest neighbor spins are parallel and cannot contribute to two-magnon scattering. The next nearest neighbor exchange interaction is much smaller than the nearest neighbor exchange interaction. The system Hamiltonian is

$$H = J \sum_{kl} \mathbf{S}_k \cdot \mathbf{S}_l. \quad (16)$$

The two-magnon scattering Hamiltonian is given by⁹⁷⁻⁹⁹

$$H_{\text{two-mag}} = \sum_{kl} A(\mathbf{e}_i \cdot \mathbf{r}_{kl})(\mathbf{e}_s \cdot \mathbf{r}_{kl})(\mathbf{S}_k \cdot \mathbf{S}_l), \quad (17)$$

where \mathbf{r}_{kl} is the unit vector connecting sites k and l sites. Here the spin longitudinal term $S_{\mathbf{R}}^z S_{\mathbf{R}+\mathbf{r}}^z$ is added to eq. (15). Two-magnon scattering is active in (aa) and (xy) and inactive in (ab) . In (xx) the two-magnon scattering Hamiltonian is the same as the system Hamiltonian except for the proportionality constant and the two-magnon scattering is inactive, because the two-magnon Hamiltonian commutes to the system Hamiltonian. The two-magnon peak energy is lower than the peak energy in the density of independent two magnon states by the magnon-magnon interaction energy J , because the exchange interaction energy between the nearest neighbor overturned spins is the same as before.

Figure 9(b) shows the stripe spin structure in BaFe_2As_2 . It should be noted that the nearest neighbor directions are x and y in BaFe_2As_2 instead of a and b in cuprate. The a and b axes are the tetragonal crystallographic axes. The nearest neighbor spin arrangement has two-fold rotational symmetry, antiparallel in the x direction and parallel in the y direction. All the second nearest neighbor spins are antiparallel. The system Hamiltonian is

$$\begin{aligned} H = & J_{1x} \sum_{\mathbf{R}, \mathbf{r}=\pm\mathbf{x}} \mathbf{S}_{\mathbf{R}} \cdot \mathbf{S}_{\mathbf{R}+\mathbf{r}} + J_{1y} \sum_{\mathbf{R}, \mathbf{r}=\pm\mathbf{y}} \mathbf{S}_{\mathbf{R}} \cdot \mathbf{S}_{\mathbf{R}+\mathbf{r}} \\ & + J_2 \sum_{\mathbf{R}, \mathbf{r}=\pm\mathbf{x}\pm\mathbf{y}} \mathbf{S}_{\mathbf{R}} \cdot \mathbf{S}_{\mathbf{R}+\mathbf{r}} \end{aligned} \quad (18)$$

The nearest and the next nearest neighbor spins should be taken into account, because both exchange interaction energies are the same order, for example, $SJ_{1x} = 36$ meV and $SJ_2 = 18$ meV.¹⁴ The two-magnon scattering Hamiltonian from the nearest neighbor

spins is given by

$$H_{\text{two-mag}}^{\text{nn}} = \sum_{r=\pm x} C e_i^x e_s^x (S_{\mathbf{R}}^+ S_{\mathbf{R}+r}^- + S_{\mathbf{R}}^- S_{\mathbf{R}+r}^+), \quad (19)$$

because only antiferromagnetic spins in the x direction can contribute to the scattering. Two-magnon scattering is active, if both incident and scattered light has the electric field component in the x direction. Then allowed polarizations are (xx) , (aa) , and (ab) . The crystals have magnetic twin structure for the interchange of x and y axes. The (yy) and (xx) polarizations cannot be distinguished. Then two-magnon scattering is inactive only in (xy) . The magnon-magnon interaction energy for the nearest neighbor spin exchange is J_{1x} .

The two-magnon scattering Hamiltonian from the second nearest neighbor spins are the same as eq. (17) of the checkerboard spin structure. The two-magnon scattering is active in (xy) and (aa) , and inactive in (ab) . The (xx) polarization is active, because the two-magnon Hamiltonian no longer commutes to the system Hamiltonian. The magnon-magnon interaction energy for the second neighbor spin exchange is J_2 .

The sum of the nearest and next nearest neighbor terms gives two-magnon intensity. Therefore it is active in all polarization configurations. In the case of antiferromagnetic J_{1x} and ferromagnetic J_{1y} the two-magnon scattering energy without the magnon-magnon interaction is the same in all polarization configurations, because the spin wave energy keeps constant along $k_y = 2\pi$ in Fig. 8(a). The magnon-magnon interaction reduces the peak energy from twice the maximum energy of the density of states by J_{1x} in (ab) and by J_2 in (xy) , because only the nearest neighbor gives scattering in (ab) and the next nearest neighbor gives scattering in (xy) . In the (aa) and (xx) spectra both components contribute.

3.3 Two-magnon scattering in BaFe_2As_2

Figure 10 shows the polarized Raman spectra in the normal state at 300 K. The broad peak at 2500 cm^{-1} is the two-magnon peak. In order to compare the two-magnon peak energies at 300 K in different polarization configurations, the intensities are adjusted so that the peak heights are the same. The spin wave densities of states calculated using eq. (10) with $J_{1x} = 36$, $J_{1y} = -7.2$, $J_2 = 18$, and $J_z = 0$ meV (black) and $J_{1x} = 17.5$, $J_{1y} = 17.5$, $J_2 = 35$, and $J_z = 0$ meV (blue) are shown in Fig. 10. The energy is doubled from that of the density of single spin wave states. It is the density of independent two magnon states. The peak energy should be higher than the

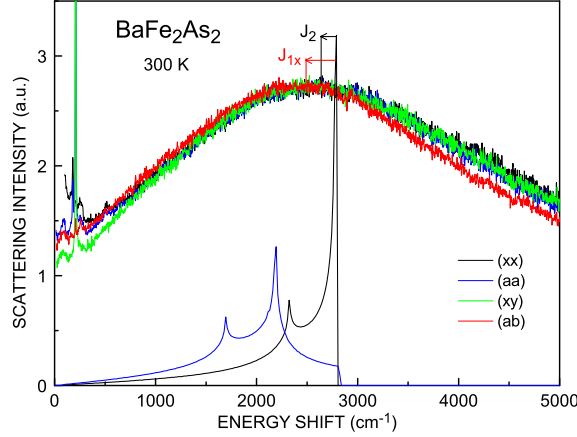


Fig. 10. (color online) Polarization configuration dependence of the two-magnon peak. The sharp curves are the density of independent two magnon states calculated using eq. (10) with the parameters $J_{1x} = 36$, $J_{1y} = -7.2$, $J_2 = 18$, and $J_z = 0$ meV (black) and $J_{1x} = 17.5$, $J_{1y} = 17.5$, $J_2 = 35$, and $J_z = 0$ meV (blue). Two-magnon scattering peak energy is lower than the peak energy in the density of independent two magnon states by the exchange interaction energy between overturned spins. The (ab) and (xy) peak energies are smaller by J_{1x} and J_2 , respectively. The (aa) and (xx) are intermediate between them.

two-magnon scattering peak energy, because the magnon-magnon interaction reduces the two-magnon scattering peak energy. Therefore the blue density of states which is obtained from the superexchange interaction model is ruled out. The peak energy in the calculated density of independent two magnon states (black) is 2790cm^{-1} .

The experimentally obtained two-magnon peak energy in the (ab) spectra is lower than the independent two magnon peak energy (black) by J_{1x} and that in the (xy) spectra is lower by J_2 . The reduced energy J_{1x} and J_2 are the expected magnon-magnon interaction energies for the (ab) and (xy) spectra assuming $S = 1$ as discussed at the end of § 3.2. In the (aa) and (xx) spectra the decreased energy is the average of J_{1x} and J_2 . The experimentally obtained peak energy of two-magnon scattering is perfectly expressed by the total energy model of the long-range stripe spin structure. The very broad peak may be attributed to the short correlation length in the metallic state. However, the large weight at the higher energy than twice the highest spin wave energy may not be explained by the above Coulomb interaction-induced model. It is discussed in the next subsection.

Very recently Chen *et al.* calculated two-magnon scattering peak energies.¹⁰⁰ The B_{1g} peak energy is a little lower than the $A_{1g} + B_{2g}$ peak energies in the model with $J_{1y} = -0.1J_{1x}$ and $J_2 = J_{1x}$ in agreement with our result. They also showed that the

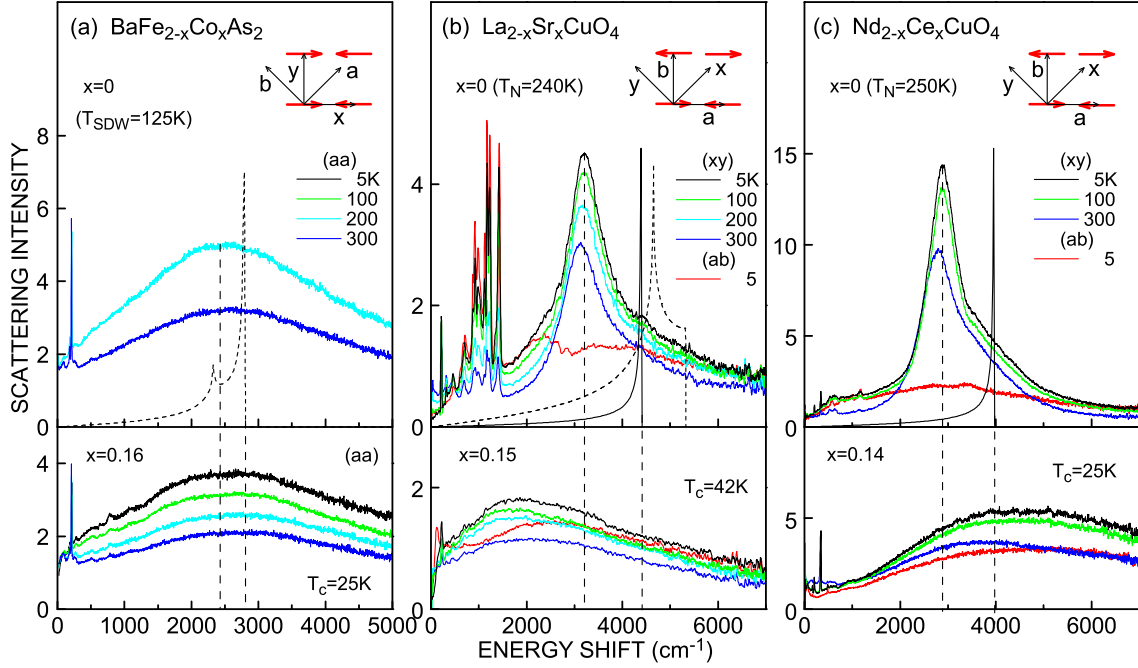


Fig. 11. (color online) (a) Temperature dependent polarized Raman spectra in the paramagnetic phase of BaFe_2As_2 (upper panel) and the superconductor $\text{BaFe}_{1.84}\text{Co}_{0.16}\text{As}_2$ (lower panel). The density of independent two magnon states is shown by the dashed line. The two-magnon peak energy and the independent two magnon excitation energy are shown by the dashed lines. The inset is the spin structure. (b) Two-magnon Raman spectra in the insulating La_2CuO_4 (upper panel) and the optimally hole-doped ($x = 0.15$) $\text{La}_{2-x}\text{Sr}_x\text{CuO}_4$ (lower panel). The density of independent two magnon states using single $J^* = 118$ meV which is obtained from the two-magnon Raman scattering is shown by the solid line and that using $J^* = 104$ and $J_2^* = -18$ meV which are obtained from neutron scattering¹⁰³ is shown by the dashed line in the upper panel. The low-energy peak at $x = 0.15$ in the (ab) spectra of $\text{La}_{2-x}\text{Sr}_x\text{CuO}_4$ is the superconducting pair breaking peak. (c) Magnetic Raman spectra in the insulating Nd_2CuO_4 (upper panel) and the electron-doped superconducting $\text{Nd}_{2-x}\text{Ce}_x\text{CuO}_4$ (lower panel). The density of independent two magnon states with $J^* = 855$ cm^{-1} is shown by the solid line.

B_{1g} peak energy with $J_2 = J_{1x} = J_{1y}$ is very low. The B_{1g} spectra observe the spin wave in k space with the weight of $(\cos k_x - \cos k_y)^2$. The energy decreases as J_2 approaches $J_{1x}/2 = J_{1y}/2$ in Fig. 8(c). However, the B_{1g} peak energy may not be so small, because the neutron scattering experiment shows $J_2 \approx 2J_{1x} = 2J_{1y}$ in the case of $J_{1x} = J_{1y}$.¹⁴

3.4 Magnetic excitations induced by moving carriers in the localized model

The magnetic Raman scattering in cuprate superconductors are considered by the localized model. Figure 11 shows the comparison among (a) iron pnictides $\text{BaFe}_{2-x}\text{Co}_x\text{As}_2$, (b) hole-doped superconductor $\text{La}_{2-x}\text{Sr}_x\text{CuO}_4$, and (c) electron-doped superconductor $\text{Nd}_{2-x}\text{Ce}_x\text{CuO}_4$. Figure 11(a) shows the antiferromagnetic metal

BaFe₂As₂ with $T_{\text{SDW}} = 130$ K and the superconductor BaFe_{1.84}Co_{0.16}As₂ with $T_c = 25$ K. The sharp dashed peak in the upper panel is the calculated density of independent two magnon states with $SJ_{1x} = 36$, $SJ_{1y} = -7.2$, and $SJ_2 = 18$ meV. The two-magnon peak remains even in electron-doped superconductor BaFe_{1.84}Co_{0.16}As₂, indicating the short-range AF magnetic correlation remains.¹¹ The two-magnon peak is very broad and has large spectral weight above twice the maximum energy of the spin wave (right dashed line). The high-energy weight cannot be interpreted by the decayed magnon in the Coulomb interaction-induced two-magnon scattering process, because the higher-order multi-magnon scattering intensity is known to be weak.¹⁰¹

In La₂CuO₄ of Fig. 11(b) the sharp peaks from 700 to 1500 cm⁻¹ are two-phonon scattering peaks. The two-magnon scattering induced by the Coulomb interaction process is active in the B_{1g} symmetry which is observed in the (xy) spectra. The rather sharp peak around 3206 cm⁻¹ at 5 K in the insulating phase is the two-magnon peak. The B_{2g} scattering intensity in the (ab) spectra is weak. If only the nearest neighbor exchange interaction is taken into account, the two-magnon peak energy is $2.76J$ ($3.38J^*$),¹⁰² where J^* is the exchange interaction energy with the correction of the quantum spin effect of $S = 1/2$ by Oguchi. The obtained J^* is 949 cm⁻¹ (118 meV). The maximum energy in the density of independent two magnon states is $4J$ ($4.63J^*$).¹⁰² The energies of the experimentally obtained two-magnon Raman peak and the independent two magnon peak are shown by the vertical dashed lines. The density of independent two magnon states calculated using single J^* is shown by the solid line in the upper panel of Fig. 11(b). Coldea *et al.*¹⁰³ obtained the full spin wave dispersion in neutron scattering. The fitted parameters are $J^* = 104$ and $J_2^* = -18$ meV, where J_2^* is the second nearest neighbor exchange interaction energy. The density of independent two magnon states is shown by the dashed line. The two-magnon scattering peak and the independent two magnon peak widely separates in the cuprates compared to BaFe₂As₂, because the spins in cuprates are $S = 1/2$ and those in iron pnictide are $S = 1$. There is small spectral weight above the independent two magnon peak energy in the insulating phase, indicating that the higher order multi-magnon scattering intensity is small.¹⁰¹ The two-magnon peak remains as temperature increases above the AF transition temperature T_N . In hole-doped La_{2-x}Sr_xCuO₄ the peak energy shifts to low energy with broadening. The magnetic scattering cannot be derived from the same process as in the insulating phase, because the integrated intensity does not decrease. If the decrease of the peak energy is caused by the shortened correlation length, the integrated intensity

decreases.¹⁰⁴

In Nd_2CuO_4 of Fig. 11(c) the two-magnon spectra in the insulating phase are nearly the same as La_2CuO_4 . The peak energy is 2890 cm^{-1} and the obtained J^* is 855 cm^{-1} . The density of independent two magnon states using only J^* is shown by the solid curve in the upper panel in Fig. 11(c). The electron doping causes the abrupt shift of the peak energy to high energy at the insulator-metal transition. The peak energy little shifts as the electron density increases in the metallic phase. The high-energy shift in the metallic phase cannot be interpreted by the Coulomb interaction induced two-magnon scattering mechanism. The spectral weights do not decrease in the metallic phase similarly to $\text{La}_{2-x}\text{Sr}_x\text{CuO}_4$. The B_{2g} spectral intensity observed in the (ab) spectra increases to nearly the same magnitude of the B_{1g} intensity in the (xy) spectra as carrier density increases. The magnetic scattering spectra in the metallic phase may be interpreted by electronic scattering with the self-energy part of the magnetic component as discussed in the following.

The electronic state of a hole moving in the AF lattice is extensively investigated in cuprates. Hopping of a hole is caused by the back-hopping of an electron with the opposite spin from the nearest neighbor site. Therefore the moving hole leaves behind an overturned spin trace in the AF spin lattice. The increased magnetic energy prevents the hole hopping. A pair of opposite spins on the trace may return to the original directions by the quantum spin fluctuation, one and a half rotation of a hole around the nearest-neighbor four Cu square sites,¹⁰⁵ the short range AF correlation, and the hopping of other holes. The electronic state was calculated, for example, by the string model taking into account the quantum spin fluctuation.⁶⁴⁻⁷¹ The hole sees a linearly rising potential on increasing the migration distance in the limit of $t \gg J$, which makes a series of discrete energy levels

$$E_n/t = -b + a_n(J/t)^{2/3}, \quad (20)$$

where a_n are the eigen values of a dimensionless Airy equation, $a_1 = 2.16$, $a_2 = 5.46$, $a_3 = 7.81$, and $b = 3.28$ at $(\pi/2, \pi/2)$.⁶⁹ The discrete peak height decreases with increasing n and connects to a continuum at high energies. The ground-state E_1 is a delta-function and the width of the second peak is about $2J$ at $J = 0.1t$. The energy difference between E_1 and E_2 is 4700 cm^{-1} using the widely accepted values of $t = 0.4 \text{ eV}$ and $J/t = 0.3$.¹⁰⁶ This energy is close to the broad peak energy in $\text{Nd}_{2-x}\text{Ce}_x\text{CuO}_4$ with $x = 0.14$. The discrete levels cannot be detected in Raman scattering, because the

levels have dispersions. The nearly constant peak energy as the carrier density increases in the metallic phase of $\text{Nd}_{2-x}\text{Ce}_x\text{CuO}_4$ is successfully explained by the string model.

In the metallic phase of the hole doped cuprate $\text{La}_{2-x}\text{Sr}_x\text{CuO}_4$, the magnetic peak energy continuously decreases with increasing the carrier density. The mean free path in the underdoped phase of the hole doped cuprate is one order shorter than that of electron doped cuprate. The migration distance is not as long as to allow the linearly rising potential approximation. The AF correlation length decreases with the increase of the hole density.¹⁰⁷ The electron Green function has a self-energy part of excited spins by the hole hopping. The electron spectral functions presented by the imaginary part of the retarded Green function has the coherent component near the original electronic energy and the incoherent component near the spin excitation energies. The $\Delta k \approx 0$ transition between the electron spectral functions gives the spectral weight at the spin excitation energies. It is in contrast to the uncorrelated electron spectral function which is presented by the delta function at the energy of the dispersion and the $\Delta k \approx 0$ transition gives only $\Delta\epsilon \approx 0$ excitations.

The very broad two-magnon peak in BaFe_2As_2 is compared to the magnetic excitation peak in the metallic cuprate. The hole density is 0.081 and the electron density is 0.069 per iron atom at 140 K in BaFe_2As_2 .⁵⁶ The spectra little changes by electron doping in $\text{BaFe}_{2-x}\text{Co}_x\text{As}_2$. The large spectral weight above the maximum of the independent two-magnon energy and the nearly independent peak energy on the electron density are similar to $\text{Nd}_{2-x}\text{Ce}_x\text{CuO}_4$. However, the peak energy is given by the two-magnon excitation energy estimated from the spin wave dispersion in BaFe_2As_2 , in contrast to the much higher energy in $\text{Nd}_{2-x}\text{Ce}_x\text{CuO}_4$.

3.5 Particle-hole excitations in the itinerant model

In the itinerant spin model the particle-hole continuum is created above the spin wave dispersion.⁶⁰⁻⁶³ The spin wave dispersion strongly decays when the energy overlaps with the particle-hole continuum. Kaneshita and Tohyama⁶² calculated the imaginary part of the susceptibility using the five-band model. The spin wave dispersion becomes clear as the magnetic moment increases. The full spin wave dispersion with the maximum energy 0.25 eV and the dispersion with the maximum energy 0.4 eV above it are obtained at the magnetic moment $M = 0.8\mu_B/\text{Fe}$. The calculation showed that the integrated intensity over k increases from energy zero to 0.2 eV. The intensity is larger in the paramagnetic phase than in the AF phase. In the Raman scattering two

particle-two hole excitations are observed. The scattering intensity decreases on increasing temperature. The increase of intensity in the paramagnetic phase is not observed. The calculation did not show whether the intensity maximum occurs at twice the top of the spin wave dispersion or not. The imaginary part of the susceptibility for the longitudinal spin excitations and the charge excitations has large intensity from 0.2 to 0.4 eV. The two particle-two hole excitations may observe from 0.4 to 0.8 eV. The observed spectra have the broad peak as shown in Fig. 11(a).

4. Conclusion

The change of the electronic and magnetic states at the SDW transition in BaFe_2As_2 was investigated by Raman scattering. The tight binding band model with two orbitals disclosed that the electronic excitations near the Dirac node and the anti-node in the SDW state have different symmetries. Utilizing this selection rule the electronic excitations near the Dirac node and the anti-node were separately obtained. The electronic excitations near the anti-node have critical fluctuation above T_{SDW} and change into the gap structure by the first order transition, while those near the Dirac node gradually changes. As for the magnetic scattering the selection rule of two-magnon scattering in the stripe spin structure was obtained. The magnetic exchange interaction energies are not presented by the superexchange interaction model, but the second derivative of the total energy of the long-range stripe spin structure with respect to the moment directions. The magnetic excitation peak survives far above T_{SDW} and in the superconductor phase of $\text{BaFe}_{2-x}\text{Co}_x\text{As}_2$, indicating that the short-range spin correlation remains in the two-dimensional magnet. The two-magnon peak energy is well understood by the conventional two-magnon scattering process in insulator. However, the high-energy spectral weight above twice the maximum energy of the spin wave may be explained by the string model in the localized spin picture or the particle-hole excitations in the itinerant picture. The difference from the high temperature superconducting cuprates were discussed.

Acknowledgment

This work was supported by E Research Project on Iron Pnictides (TRIP), Japan Science and Technology Agency (JST).

References

- 1) Y. Kamihara, T. Watanabe, M. Hirano, and H. Hosono, *J. Am. Chem. Soc.* **130** (2008) 3296.
- 2) Z.-A. Ren, G.-C. Che, X.-L. Dong, J. Yang, W. Lu, W. Yi, X.-L. Shen, Z.-C. Li, L.-L. Sun, F. Zhou, and Z.-X. Zhao: *Europhys. Lett.* **83** (2008) 17002.
- 3) G. F. Chen, Z. Li, D. Wu, G. Li, W. Z. Hu, J. Dong, P. Zheng, J. L. Luo, and N. L. Wang: *Phys. Rev. Lett.* **100** (2008) 247002.
- 4) M. Rotter, M. Tegel, .D. Johrendt, I. Schellenberg, W. Hermes, and R. Pöttgen: *Phys. Rev. B* **78** (2008) 020503(R).
- 5) M. Rotter, M. Tegel, and D. Johrendt: *Phys. Rev. Lett.* **101** (2008) 107006.
- 6) M. S. Torikachvili, S. L. Bud'ko, N. Ni, and P. C. Canfield: *Phys. Rev. Lett.* **101** (2008) 057006.
- 7) T. Thio, T. R. Thurston, W. Preyer, P. J. Picone, M. A. Kastner, H. P. Jenssen, D. R. Gabbe, C. Y. Chen, R. J. Birgeneau, and A. Aharony: *Phys. Rev.* **38** (1988) 905.
- 8) M. Ishikado, R. Kajimoto, S. Shamoto, M. Arai, A. Iyo, K. Miyazawa, P. M. Shirage, H. Kito, H. Eisaki, S. Kim, H. Hosono, T. Guidi, R. Bewley, and S. M. Bennington: *J. Phys. Soc. Japan*, **78** (2009) 043705.
- 9) S. O. Diallo, D. K. Pratt, R. M. Fernandes, W. Tian, J. L. Zarestky, M. Lumsden, T. G. Perring, C. L. Broholm, N. Ni, S. L. Bud'ko, P. C. Canfield, H.-F. Li, D. Vaknin, A. Kreyssig, A. I. Goldman, and R. J. McQueeney: *Phys. Rev. B* **81** (2010) 214407.
- 10) K. Matan, R. Morinaga, K. Iida, and T. J. Sato: *Phys. Rev. B* **79** (2009) 054526.
- 11) S. Sugai, Y. Mizuno, K. Kiho, M. Nakajima, C. H. Lee, A. Iyo, H. Eisaki, and S. Uchida: *Phys. Rev. B* **82** (2010) 140504(R).
- 12) K. Okazaki, S. Sugai, S. Niitaka, and H. Takagi: *Phys. Rev. B* **83** (2011) 035103.
- 13) K. Kaneko, A. Hoser, N. Caroca-Canales, A. Jesche, C. Krellner, O. Stockert, and C. Geibel: *Phys. Rev. B* **78** (2008) 212502.
- 14) R. A. Ewings, T. G. Perring, R. I. Bewley, T. Guidi, M. J. Pitcher, D. R. Parker, S. J. Clarke, and A. T. Boothroyd: *Phys. Rev. B* **78** (2008) 220501(R).

- 15) A. I. Goldman, D. N. Argyriou, B. Ouladdiaf, T. Chatterji, A. Kreyssig, S. Nandi, N. Ni, S. L. Bud'ko, P. C. Canfield, and R. J. McQueeney: Phys. Rev. B **78** (2008) 100506(R).
- 16) M. D. Johannes and I. I. Mazin: Phys. Rev. B **79** (2009) 220510(R).
- 17) Q. Huang, Y. Qiu,^{1,2} Wei Bao, M. A. Green, J.W. Lynn, Y. C. Gasparovic, T. Wu, G. Wu, and X. H. Chen: Phys. Rev. Lett. **101** (2008) 257003.
- 18) S. O. Diallo, V. P. Antropov, T. G. Perring, C. Broholm, J. J. Pulikkotil, N. Ni, S. L. Bud'ko, P. C. Canfield, A. Kreyssig, A. I. Goldman, and R. J. McQueeney: Phys. Rev. Lett. **102** (2009) 187206.
- 19) I. I. Mazin, D. J. Singh, M. D. Johannes, and M. H. Du: Phys. Rev. Lett. **101** (2008) 057003.
- 20) K. Kuroki, S. Onari, R. Arita, H. Usui, Y. Tanaka, H. Kontani, and H. Aoki: Phys. Rev. Lett. **101** (2008) 087004.
- 21) J. Dong, H. J. Zhang, G. Xu, Z. Li, G. Li, W. Z. Hu, D. Wu, G. F. Chen, X. Dai, J. L. Luo, Z. Fang, and N. L. Wang: Europhys. Lett. **83** (2008) 27006.
- 22) H. Ding, P. Richard, K. Nakayama, K. Sugawara, T. Arakane, Y. Sekiba, A. Takayama, S. Souma, T. Sato, T. Takahashi, Z. Wang, X. Dai, Z. Fang, G. F. Chen, J. L. Luo, and N. L. Wang: Europhys. Lett. **83** (2008) 47001.
- 23) K. Terashima, Y. Sekiba, J. H. Bowen, K. Nakayama, T. Kawahara, T. Sato, P. Richard, Y.-M. Xu, L. J. Li, G. H. Cao, Z.-A. Xu, H. Ding, and T. Takahashi: Proceedings of the National Academy of Sciences of the United States of America, **106**, No. 18 (2009) 7330.
- 24) S. Li, C. de la Cruz, Q. Huang, Y. Chen, J. W. Lynn, J. Hu, Y.-L. Huang, F.-C. Hsu, K.-W. Yeh, M.-K. Wu, and P. Dai: Phys. Rev. B **79** (2009) 054503.
- 25) W. Bao, Y. Qiu, Q. Huang, M. A. Green, P. Zajdel, M. R. Fitzsimmons, M. Zherrenkov, S. Chang, M. Fang, B. Qian, E. K. Vehstedt, J. Yang, H. M. Pham, L. Spinu, and Z. Q. Mao: Phys. Rev. Lett. **102** (2009) 247001.
- 26) F. Wang, H. Zhai, Y. Ran, A. Vishwanath, and D.-H. Lee: arXis:0805.3343.
- 27) Y. Ran, F. Wang, H. Zhai, A. Vishwanath, and D.-H. Lee: Phys. Rev. B **79** (2009) 014505.
- 28) N. Harrison and S. E. Sebastian: Phys. Rev. B **80** (2009) 224512.

- 29) T. Morinari, E. Kaneshita, and T. Tohyama: Phys. Rev. Lett. **105** (2010) 037203.
- 30) J. Zhao, D.-X. Yao, S. Li, T. Hong, Y. Chen, S. Chang, W. Ratcliff II, J.W. Lynn, H. A. Mook, G. F. Chen, J. L. Luo, N. L. Wang, E.W. Carlson, J. Hu, and P. Dai: Phys. Rev. Lett. **101** (2008) 167203.
- 31) T. Yildirim: Phys. Rev. Lett. **101** (2008) 057010,
- 32) Z. P. Yin, S. Lebègue, M. J. Han, B. P. Neal, S.Y. Savrasov, and W. E. Pickett: Phys. Rev. Lett. **101** (2008) 047001,
- 33) Q. Si and E. Abrahams: Phys. Rev. Lett. **101** (2008) 076401,
- 34) M. J. Han, Q. Yin, W. E. Pickett, and S. Y. Savrasov: Phys. Rev. Lett. **102** (2009) 107003.
- 35) J K Dong, L Ding, H Wang, X F Wang, T Wu, G Wu², X H Chen and S Y Li: New J. Phys. **10** (2008) 123031.
- 36) J.-H. Chu, J. G. Analytis, C. Kucharczyk, and I. R. Fisher: Phys. Rev. B **79** (2009) 014506.
- 37) K. Kitagawa, N. Katayama, K. Ohgushi, and M. Takigawa: J. Phys. Soc. Japan, **78** (2009) 063706.
- 38) S.-H. Baek, N. J. Curro, T. Klimczuk, E. D. Bauer, F. Ronning, and J. D. Thompson: Phys. Rev. B **79** (2009) 052504.
- 39) M. A. Tanatar, N. Ni, G. D. Samolyuk, S. L. Bud'ko, P. C. Canfield, and R. Prozorov: Phys. Rev. B **79** (2009) 134528.
- 40) C. de la Cruz, Q. Huang, J. W. Lynn, J. Li, W. Ratcliff II, J. L. Zarestky, H. A. Mook, G. F. Chen, J. L. Luo, N. L. Wang, and P. Dai: Nature, **453** (2008) 899.
- 41) R. J. McQueeney, S. O. Diallo, V. P. Antropov, G. D. Samolyuk, C. Broholm, N. Ni, S. Nandi, M. Yethiraj, J. L. Zarestky, J. J. Pulikkotil, A. Kreyssig, M. D. Lumsden, B. N. Harmon, P. C. Canfield, and A. I. Goldman: Phys. Rev. Lett. **101** (2008) 227205.
- 42) X.-L. Qi, S. Raghu, C.-X. Liu, D. J. Scalapino and S.-C. Zhang: arXiv:0804.4332.
- 43) S. Raghu, X.-L. Qi, C.-X. Liu, D. J. Scalapino, and S.-C. Zhang: Phys. Rev. B **77** (2008) 220503(R).
- 44) S. Graser, T. A. Maier, P. J. Hirschfeld, and D. J. Scalapino: New J. Phys. **11** (2009) 025016.
- 45) O. K. Andersen and L. Boeri: Ann. Phys. (Berlin) **523** (2011) 8.

- 46) I. Eremin and A. V. Chubukov: Phys. Rev. B **81** (2010) 024511.
- 47) P. Richard, K. Nakayama, T. Sato, M. Neupane, Y.-M. Xu, J. H. Bowen, G. F. Chen, J. L. Luo, N. L. Wang, X. Dai, Z. Fang, H. Ding, and T. Takahashi: Phys. Rev. Lett. **104** (2010) 137001.
- 48) K. S. Novoselov, A. K. Geim, S. V. Morozov, D. Jiang, M. I. Katsnelson, I. V. Grigorieva, S. V. Dubonos, and A. A. Firsov: Nature, **438** (2005) 197.
- 49) S. Sugai, Y. Mizuno, R. Watanabe, T. Kawaguchi, K. Takenaka, H. Ikuta, Y. Takayanagi, N. Hayamizu, and Y. Sone: arXiv:1010.6151.
- 50) L. Chauvière, Y. Gallais, M. Cazayous, M. A. Méasson, A. Sacuto, D. Colson, and A. Forget: Phys. Rev. B **82** (2010) 180521(R).
- 51) W. Z. Hu, J. Dong, G. Li, Z. Li, P. Zheng, G. F. Chen, J. L. Luo, and N. L. Wang: Phys. Rev. Lett. **101** (2008) 257005.
- 52) L. X. Yang, Y. Zhang, H. W. Ou, J. F. Zhao, D. W. Shen, B. Zhou, J. Wei, F. Chen, M. Xu, C. He, Y. Chen, Z. D. Wang, X. F. Wang, T. Wu, G. Wu, X. H. Chen, M. Arita, K. Shimada, M. Taniguchi, Z. Y. Lu, T. Xiang, and D. L. Feng: Phys. Rev. Lett. **102** (2009) 107002.
- 53) Y. Zhang, J. Wei, H. W. Ou, J. F. Zhao, B. Zhou, F. Chen, M. Xu, C. He, G. Wu, H. Chen, M. Arita, K. Shimada, H. Namatame, M. Taniguchi, X. H. Chen, and D. L. Feng: Phys. Rev. Lett. **102** (2009) 127003,
- 54) C. Liu, T. Kondo, N. Ni, A. D. Palczewski, A. Bostwick, G. D. Samolyuk, R. Khasanov, M. Shi, E. Rotenberg, S. L. Bud'ko, P. C. Canfield, and A. Kaminski: Phys. Rev. Lett. **102** (2009) 167004.
- 55) J. Fink, S. Thirupathaiah, R. Ovsyannikov, H. A. Dürr, R. Follath, Y. Huang, S. de Jong, M. S. Golden, Y.-Z. Zhang, H. O. Jeschke, R. Valentí, C. Felser, S. D. Farahani, M. Rotter, and D. Johrendt: Phys. Rev. B **79** (2009) 155118.
- 56) M. Yi, D. H. Lu, J. G. Analytis, J.-H. Chu, S.-K. Mo, R.-H. He, M. Hashimoto, R. G. Moore, I. I. Mazin, D. J. Singh, Z. Hussain, I. R. Fisher, and Z.-X. Shen: Phys. Rev. B **80** (2009) 174510.
- 57) M. Yi, D. H. Lu, J. G. Analytis, J.-H. Chu, S.-K. Mo, R.-H. He, R. G. Moore, X. J. Zhou, G. F. Chen, J. L. Luo, N. L. Wang, Z. Hussain, D. J. Singh, I. R. Fisher, and Z.-X. Shen: Phys. Rev. B **80** (2009) 024515.

- 58) C. Lester, J.-H. Chu, J. G. Analytis, T. G. Perring, I. R. Fisher, and S. M. Hayden: Phys. Rev. B **81** (2010) 064505.
- 59) J. Zhao, D. T. Adroja, D.-X. Yao, R. Bewley, S. Li, X. F. Wang, G. Wu, X. H. Chen, J. Hu, and P. Dai: Nature Phys. **5** (2009) 555.
- 60) T. Kariyado and M. Ogata: J. Phys. Soc. Japan, **78** (2009) 043708.
- 61) P. M. R. Brydon and C. Timm: Phys. Rev. B **80** (2009) 174401.
- 62) E. Kaneshita and T. Tohyama: Phys. Rev. B **82** (2010) 094441.
- 63) J. Knolle, I. Eremin, A. V. Chubukov, and R. Moessner: Phys. Rev. B **81** (2010) 140506(R).
- 64) W. F. Brinkman and T. M. Rice: Phys. Rev. B **2** (1970) 1324.
- 65) B. I. Shraiman and E. D. Siggia: Phys. Rev. Lett. **61** (1988) 467.
- 66) F. Marsiglio, A. E. Ruckenstein, S. Schmitt-Rink, and C. M. Varma: Phys. Rev. B **43** (1991) 10882.
- 67) E. Dagotto, R. Joynt, A. Moreo, S. Bacci, and E. Gagliano: Phys. Rev. B **41** (1990) 9049.
- 68) G. Martinez and P. Horsch: Phys. Rev. B **44** (1991) 317.
- 69) Z. Liu and E. Manousakis: Phys. Rev. B **45** (1992) 2425.
- 70) P. A. Lee, N. Nagaosa, and X.-G. Wen: Rev. Mod. Phys. **78** (2006) 17.
- 71) E. Manousakis: Phys. Rev. B **75** (2007) 035106.
- 72) P. A. Wolff: Phys. Rev. Lett., **16** (1966) 225.
- 73) P. M. Platzman and N. Tzoar: Phys. Rev. **182** (1969) 510.
- 74) M. V. Klein and S. B. Dierker: Phys. Rev. B **29** (1984) 4976.
- 75) M. Cardona: Physica C **317-318** (1999) 30.
- 76) I. I. Mazin, T. P. Devereaux, J. G. Analytis, J.-H. Chu, I. R. Fisher, B. Muschler, and R. Hackl: Phys. Rev. B **82** (2010) 180502(R).
- 77) B. Muschler, W. Prestel, R. Hackl, T. P. Devereaux, J. G. Analytis, J.-H. Chu, and I. R. Fisher: Phys. Rev. B **80** (2009) 180510(R).
- 78) A. Moreo, M. Daghofer, J. A. Riera, and E. Dagotto: Phys. Rev. B **79** (2009) 134502.
- 79) J. Zhang, R. Sknepnek, R. M. Fernandes, and J. Schmalian: Phys. Rev. B **79** (2009) 220502(R).

- 80) A. P. Litvinchuk, V. G. Hadjiev, M. N. Iliev, Bing Lv, A. M. Guloy, and C. W. Chu: Phys. Rev. B **78** (2008) 060503(R).
- 81) M. Rahlenbeck, G. L. Sun, D. L. Sun, C. T. Lin, B. Keimer, and C. Ulrich: Phys. Rev. B **80** (2009) 064509.
- 82) K.-Y. Choi, D. Wulferding, P. Lemmens, N. Ni, S. L. Bud'ko, and P. C. Canfield: Phys. Rev. B **78** (2008) 212503.
- 83) L. Chauvière, Y. Gallais, M. Cazayous, A. Sacuto, and M. A. Méasson: Phys. Rev. B **80** (2009) 094504.
- 84) E. Kaneshita, T. Morinari, and T. Tohyama: Phys. Rev. Lett. **103** (2009) 247202.
- 85) S. Graser, A. F. Kemper, T. A. Maier, H.-P. Cheng, P. J. Hirschfeld, and D. J. Scalapino: Phys. Rev. B **81** (2010) 214503.
- 86) G. D. Mahan: *Many-Particle Physics*, (Kluwer Academic/Plenum Publishers, New York, 2000).
- 87) C. Cao, P. J. Hirschfeld, and H.-P. Cheng: Phys. Rev. B **77** (2008) 220506(R).
- 88) H. Ikeda, R. Arita, and J. Kuneš: Phys. Rev. B **81** (2010) 054502.
- 89) K. Kuroki, H. Usui, S. Onari, R. Arita, and H. Aoki: Phys. Rev. B **79** (2009) 224511.
- 90) A. Akrap, J. J. Tu, L. J. Li, G. H. Cao, Z. A. Xu, and C. C. Homes: Phys. Rev. B **80** (2009) 180502(R).
- 91) N. Ni, M. E. Tillman, J.-Q. Yan, A. Kracher, S. T. Hannahs, S. L. Bud'ko, and P. C. Canfield: Phys. Rev. B **78** (2008) 214515.
- 92) A. J. Drew, Ch. Niedermayer, P. J. Baker, F. L. Pratt, S. J. Blundell, T. Lancaster, R. H. Liu, G. Wu, X. H. Chen, I. Watanabe, V. K. Malik, A. Dubroka, M. Rössle, K.W. Kim, C. Baines, and C. Bernhard: Nature Materials, **8** (2009) 310.
- 93) R. M. Fernandes, D. K. Pratt, W. Tian, J. Zarestky, A. Kreyssig, S. Nandi, M. G. Kim, A. Thaler, N. Ni, P. C. Canfield, R. J. McQueeney, J. Schmalian, and A. I. Goldman: Phys. Rev. B **81** (2010) 140501(R).
- 94) T. Moriya: J. Appl. Phys. **39** (1968) 1042.
- 95) P. A. Fleury, S. P. S. Porto, and R. Loudon: Phys. Rev. Lett. **18** (1967) 658.
- 96) P. A. Fleury: Phys. Rev. Lett. **21** (1968) 151.
- 97) R. J. Elliott, M. F. Thorpe, G. F. Imbusch, R. Loudon, and J. B. Parkinson: Phys. Rev. Lett. **21** (1968) 147.

- 98) R. J. Elliott, M. F. Thorpe: J. Phys. C (Solid St. Phys.), Ser 2, **2** (1969) 1630.
- 99) J. B. Parkinson: J. Phys. C (Solid St. Phys.), Ser 2, **2** (1969) 2012.
- 100) C.-C. Chen, C. J. Jia, A. F. Kemper, R. R. P. Singh, and T. P. Devereaux: Phys. Rev. Lett. **106** (2011) 067002.
- 101) R. R. P. Singh, P. A. Fleury, K. B. Lyons, and P. E. Sulewski: Phys. Rev. Lett. **62** (1989) 2736.
- 102) C. M. Canali and S. M. Girvin: Phys. Rev. B **45** (1992) 7127.
- 103) R. Coldea, S. M. Hayden, G. Aeppli, T. G. Perring, C. D. Frost, T. E. Mason, S.-W. Cheong, and Z. Fisk, Phys. Rev. Lett. **86** (2001) 5377.
- 104) T. Tohyama: Phys. Rev. B **70** (2004) 174517.
- 105) S. A. Trugman: Phys. Rev. B **37** (1988) 1597.
- 106) C. Kim, P. J. White, Z.-X. Shen, T. Tohyama, Y. Shibata, S. Maekawa, B. O. Wells, Y. J. Kim, R. J. Birgeneau, and M. A. Kastner: Phys. Rev. Lett. **80** (1998) 4245.
- 107) R. J. Birgeneau, D. R. Gabbe, H. P. Jenssen, M. A. Kastner, P. J. Picone, T. R. Thurston, G. Shirane, Y. Endoh, M. Sato, K. Yamada, Y. Hidaka, M. Oda, Y. Enomoto, M. Suzuki, and T. Murakami: Phys. Rev. B **38** (1988) 6614.